A novel approach to localize cortical TMS effects

Konstantin Weise[1,2+*], Ole Numssen[3+], Axel Thielscher[4,5], Gesa Hartwigsen[3#], Thomas R. Knösche[1,6#]

[1]Max Planck Institute for Human Cognitive and Brain Sciences, Stephanstr. 1a, 04103 Leipzig, Germany.

[2]Technische Universität Ilmenau, Advanced Electromagnetics Group, Helmholtzplatz 2, 98693 Ilmenau, Germany.

[3]Research Group Modulation of Language Networks, Department of Neuropsychology, Max Planck Institute for Human Cognitive and Brain Sciences, Stephanstr. 1a, 04103 Leipzig, Germany.

[4]Danish Research Centre for Magnetic Resonance, Centre for Functional and Diagnostic Imaging and Research, Copenhagen University Hospital Hvidovre, Denmark.

[5]Technical University of Denmark, Center for Magnetic Resonance, Department of Electrical Engineering, Kongens Lyngby, Denmark.

[6]Technische Universität Ilmenau, Institute of Biomedical Engineering and Informatics, Gustav-Kirchhoff-Straße 2, 98693 Ilmenau, Germany.

[+,#] contributed equally

* CORRESPONDING AUTHOR

Konstantin Weise; Max Planck Institute for Human Cognitive and Brain Sciences, Stephanstr. 1a, 04103 Leipzig, Germany; Technische Universität Ilmenau, Advanced Electromagnetics Group, Helmholtzplatz 2, 98693 Ilmenau, Germany; e-mail: kweise@cbs.mpg.de, phone: +49 341 9940-2580

ABSTRACT

Despite the widespread use of transcranial magnetic stimulation (TMS), its precise cortical location underlying the physiological and behavioral stimulation effects are still only coarsely known. So far, mapping strategies that systematically measure TMS effects rely on center of gravity approaches and therefore localize the stimulated cortical site only approximately and indirectly. Focusing on the motor cortex, we present a new method to reliably determine the stimulated cortical site at the individual subject level. The approach combines measurements of motor evoked potentials (MEPs) at different coil positions and orientations with numerical modeling of induced electric fields. We identify sharply bounded cortical areas around the gyral crowns and rims of the motor hand area as the origin of the MEPs and show that the tangential field component and the magnitude of the electric field is most relevant for the observed effect. The identification requires relatively few measurements at different coil positions and orientations. We use extensive uncertainty and sensitivity analyses to verify the robustness of the method and identify the most critical model parameters. Our approach improves the localization of the cortex area stimulated by TMS. It is generic and can potentially be applied to other modalities such as language mapping.

KEYWORDS

Brain mapping; Finite element analysis; Motor cortex; Transcranial magnetic stimulation; Uncertainty and sensitivity analysis;

1 INTRODUCTION

Transcranial magnetic stimulation (TMS) is capable of modulating motor and cognitive functions in the human brain. An important application of this technique is mapping structure-function relationships (see Bestmann and Feredoes, 2013; Sandrini et al., 2011; Siebner et al., 2009 for review). Such mappings are not only of fundamental neuroscientific interest, but also have practical clinical relevance, for example in the context of presurgical mapping. In a classical mapping study, the TMS coil is systematically moved over a grid of positions and/or orientations while certain behavioral or physiological variables (e.g., the degree of speech impairment or the magnitude of motor evoked potentials) are observed (Picht, 2014). The coil position/orientation producing the best fitting output is then used as a proxy for the brain structures underlying the targeted effects, either in a simple way by direct projection onto the cortical surface (Krieg et al., 2014) or more sophisticated by calculation of the induced electric fields (Tarapore et al, 2013). This approach has some principal shortcomings. First, it is only limitedly capable of unambiguously determining the location and orientation of the stimulated neural structures. Even if the coil configuration associated with the optimal output can be found accurately, it generates electric fields in a wide range of neural structures, such as radial cells in several parallel sulcal walls and tangential structures (e.g., axons) in gyral crowns. The field maximum does not reliably indicate which of these components is actually driving the effect. Second, because the search space has at least 3 dimensions (2 for position on head surface, 1 for coil orientation), accurate mapping may require a very large number of repetitions to avoid undersampling. Consequently, previous studies remain controversial on fundamental aspects of the physiological TMS effects and their localization on the cortical surface. For instance, it is still unclear which part of the primary motor cortex is effectively stimulated by the TMS pulse (see Bungert et al., 2017; Laakso et al., 2018; Fox et al., 2004; Krieg et al., 2013), precluding strong conclusions on the cortical origin of the TMS effect. In particular, previous studies remain controversial with respect to the contribution of the gyral crowns and sulcal walls in the primary motor cortex (see Fox et al., 2004; Bungert et al., 2017; Opitz et al., 2013; Laakso et al., 2018; Krieg et al., 2013).

Resolving these limitations and establishing a link between coil position and location and size of affected cortical area in three dimensions (i.e., also in depth) is not trivial. It requires

detailed estimates of the electric field pattern on the individual level, biophysically motivated hypotheses on the mechanism of action by which the electric field causes neural excitation, and formal statistical testing to demonstrate the validity of the obtained results.

The induced electric field distribution in the brain strongly depends on several stimulation parameters such as stimulation intensity, location, and orientation of the TMS coil as well as the complex individual geometry of the brain (Thielscher et al., 2011), and several biophysical parameters, such as tissue conductivities and fractional anisotropy. Recently, numerical modeling of the induced electric field has been increasingly used (Bestmann, 2015; Thielscher et al., 2011; Thielscher et al., 2015), but has not become a standard procedure in medical applications so far. In particular, calculations based on subject-specific head meshes have improved our understanding of the impact of the individual head anatomy on the field distribution (Datta et al., 2010; Thielscher et al., 2011) (e.g. De Lucia et al., 2007; Opitz et al., 2013; Opitz et al., 2011; Opitz et al., 2014; Thielscher et al., 2011). As such, numerical field calculations using anatomically detailed head models may assist the neurobiological interpretation of TMS effects, and aid the localization of the stimulated cortical area that underlies the observed physiological or behavioral effect (see Hartwigsen et al., 2015; Bungert 2017). However, since a TMS pulse induces a distributed electric field over an extended part of the cortex, it is difficult to determine where exactly the neural activation occurs, even if the field can be computed reliably.

Moreover, any approach that aims to make beneficial use of field models to improve localization has to account for the uncertainties of the numerical simulations to yield accurate and robust conclusions. Uncertainties are particularly caused by the assumed ohmic tissue conductivities, which are only coarsely known. Such an approach also has to be able to deal with uncertainties caused by the limited knowledge on how the induced field acts on different neuron types. Recently, field calculations have been combined with microscopic neural models based on accurate reconstructions from histology (Seo et al., 2017; Aberra et al. 2018). However, for now, data validating these models is largely missing and the conclusions depend strongly on model details such as the types of the included neural elements, thereby differing between studies.

We introduce a novel TMS mapping approach that links biophysical modeling of the induced electric field with physiological measurements within a principled statistical testing framework to determine the stimulated cortical area on an individual level. It is based on the assumption of a unique functional relationship between an observed physiological TMS effect and the electric field induced at the cortical location that underlies this effect. Given an experimental effect that linearly or non-linearly scales with the stimulation intensity, it can be assumed that this effect also scales with the degree of excitation of the specific neuronal population, which is functionally linked to it. Hence, the functional relationship between the electric field component that coincides spatially and orientation-wise with this population and the observed effect should be invariant across experimental conditions with different orientations and positions of the TMS coil. The task of localizing the stimulated cortical area can thus be solved by determining the brain area in which the induced field shows a clear functional relationship to the recorded effects. Note that this area does not have to coincide with the field maximum. Similar, but more restricted localization approaches have been used in previous studies. Targeting the hand area of the primary motor cortex, Bungert et al. (2017) employed a statistical approach based on the experimentally determined motor thresholds (MTs) at different coil orientations. Laakso et al. (2018) used a similar strategy, but investigated the influence of different coil positions while keeping the orientation constant. These studies demonstrated the principal validity of the rationale to localize the stimulated cortical area using the functional relationship between calculated fields and the observed effects. However, they remain restricted in several important aspects. First, the ability for a precise functional localization on the single-subject level was not demonstrated. Second, it remains unknown how many experimental conditions are needed to achieve a good localization result and how these positions and orientations should be chosen. Third, the robustness of the approaches to inevitable uncertainties in the tissue conductivities was not examined.

Our new approach differs from these prior studies in two important aspects to advance localization on the single-subject level: 1) It combines multiple stimulations with different coil positions and orientations. 2) instead of using the MT, it exploits entire input-output curves (I/O curves; relationship between stimulation intensity and MEP amplitude) (Fig. 1). We show that it provides a means of precisely localizing the individual cortical area that is responsible

for the observed motor output. We prove its stability and robustness using comprehensive permutation tests and a rigorous uncertainty and sensitivity analysis based on the generalized polynomial chaos (gPC) approach [Le Maitre et al. 2010]. To account for the limited knowledge on the neural target structures of TMS, we tested several components of the induced field, and consistently found the tangential field component and the field magnitude to be the relevant quantities for modulating the observed effect. Importantly, we demonstrate that unique results can be obtained with relatively few measurements and give indications how the respective coil positions and orientations should be chosen. Our approach improves the localization of effectively stimulated areas during TMS. While demonstrated for the motor cortex, it is generic and can be applied to mapping approaches in other domains such as language.

2 MATERIALS AND METHODS

We developed a framework to localize the neuronal populations that are responsible for effects of TMS by combining behavioral responses with numerical modeling and applied this to motor cortex stimulation and electrophysiological measurements of muscle activation. First, the experimental design to elicit and measure MEPs is described. Secondly, we show how to calculate the TMS induced electric field distribution in the subjects' heads. This covers models for the head, the TMS coils, as well as the differential equations numerically solved to determine the electric field inside the brain. Thirdly, we present a new measure to quantify the correlation between the induced electric field and the behavioral or physiological stimulation effect, the congruence factor. Locations with high congruence are likely to house neural populations that are causally linked to the observed MEP. Finally, the results are analyzed in terms of their sensitivity towards uncertain model parameters such as the electrical conductivities of the brain tissues and the measured MEPs using a generalized polynomial chaos (gPC) approach.

2.1 TMS Experiments

The principal experimental setup is shown in Fig. 1. Fifteen healthy, right-handed participants (seven female, age 22-34 years) were recruited. The mean laterality index according to the Edinburgh Handedness Inventory (Oldfield 1971) was 92.93 (SD = 10.66). Subject inclusion was in accordance with the published guidelines on patient selection for TMS

166 studies (Rossi et al., 2009, p. 2025). Written informed consent was obtained from all
167 participants prior to the examination. The study was performed according to the guidelines of
168 the Declaration of Helsinki and approved by the local Ethics committee of the Medical Faculty
169 of the University of Leipzig.

170 Stimulation was applied with a MagPro X100 stimulator (MagVenture, firmware Version
171 7.1.1) and CB-60 figure-of-eight coils, guided by a neuronavigation system (software: Localite,
172 Germany, Sankt Augustin; camera: Polaris Spectra, NDI, Canada, Waterloo).

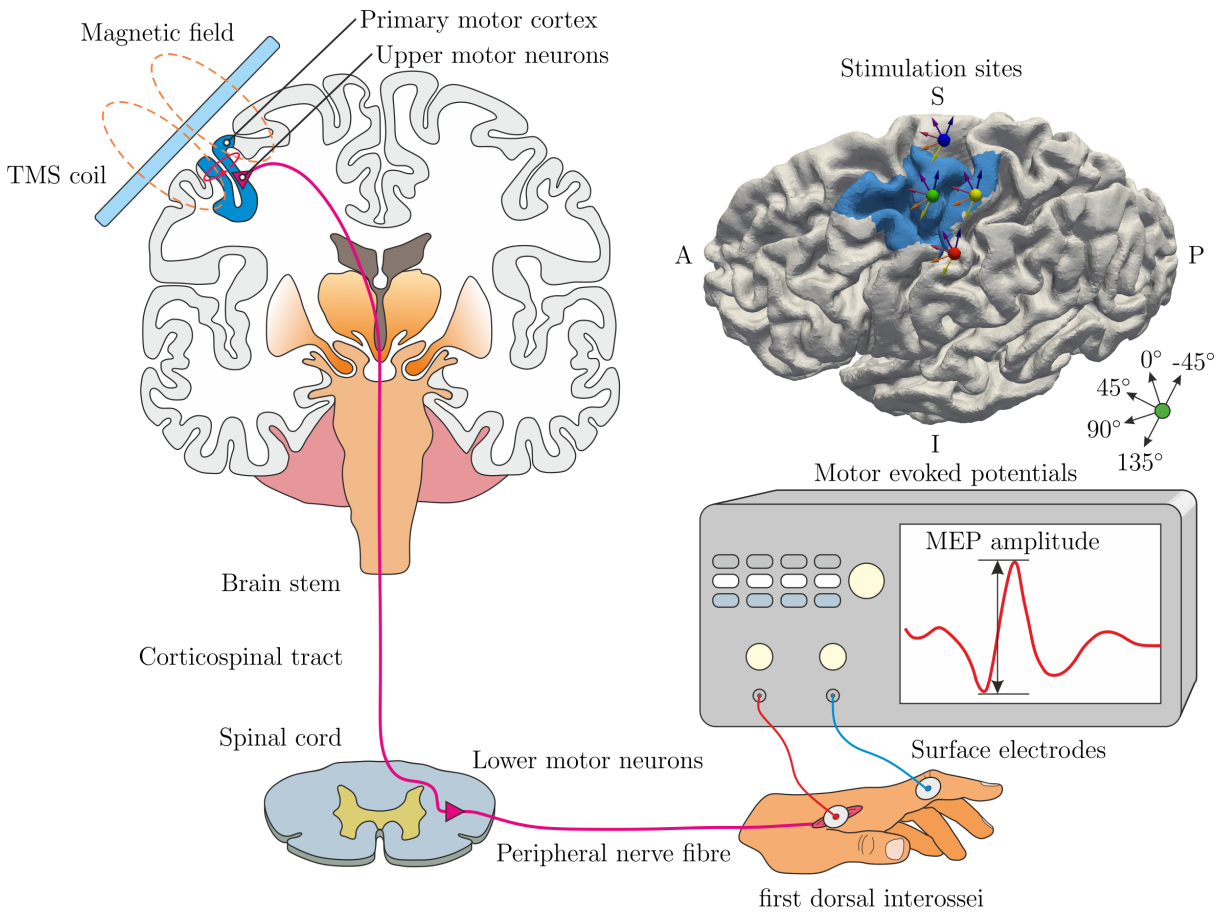

Figure 1: Schematic representation of the experimental procedure of the TMS experiments. Top left: The TMS coil is located tangentially to the skull over the primary motor cortex (M1). A time changing current in the coil generates a time changing magnetic field, which induces an electric field in the brain. This depolarizes the upper motor neurons with corticospinal efferents. Bottom: Action potentials from the upper motor neurons excite the lower motor neurons in the spinal cord, whose action potentials travel through the peripheral nerves to the first dorsal interossei (FDI) of the hand. The muscle responses (motor-evoked potentials, MEP) are measured using a classical belly tendon montage, i.e. between the dorsal interosseus and proximal interphalangeal joint of the index finger. Top right: example cortical surface with region of interest (blue), showing positions of the coil centers (colored balls) and the coil orientations (arrows) for the 20 experimental conditions.

173 MEPs were recorded at the subjects' right hand index fingers with one surface electrode
174 positioned over the muscle belly of the FDI and one at the proximal interphalangeal joint (PIP).
175 The electrodes were connected to a patient amplifier system (D-360, DigitimerLtd., UK,
176 Welwyn Garden City; bandpass filtered from 10 Hz to 2 kHz), which in turn was connected to a
177 data acquisition interface (Power1401 MK-II, CED Ltd., UK, Cambridge, 2 kHz sampling rate).
178 Stimulation control and recording was performed with Signal (CED Ltd., version 4.11).

179 Localization of the MEP stimulation hotspot was guided by individually transformed M1
180 coordinates based on the standardized group coordinates from Mayka et al. (2006). These
181 coordinates were transferred to the individual subject's brain by using the inverse of the
182 normalization transformation in SPM8 (https://www.fil.ion.ucl.ac.uk/spm/) (Penny et al. 2007).
183 The individual MEP producing hotspot $M1_{45°}$ and its corresponding resting motor threshold
184 ($MT_{M1_{45°}}$) were determined. $MT_{M1_{45°}}$ was defined as the minimum stimulation intensity, which
185 still evokes MEPs with an amplitude of at least 50 µV in at least 5 out of 10 consecutive
186 stimulations (Pascual-Leone and Torres, 1993; Rothwell et al., 1999; Conforto et al. 2004).
187 In relation to $M1_{45°}$, five additional conditions, shown in Fig. 2(a), with different stimulation
188 sites and coil orientations were defined in the following way. In Experiment I, the TMS coil was
189 located over M1 and 2 cm posterior (P). At both sites, three coil orientations with respect to
190 $M1_{45°}$ were investigated, namely $M1_{0°}/P_{0°}$ (-45° from $M1_{45°}$), $M1_{45°}/P_{45°}$, and $M1_{90°}/P_{90°}$ (+45°
191 from $M1_{45°}$), resulting in six experimental conditions.

192 Experiment II included three of the original fifteen subjects and the number of conditions
193 was increased to further investigate the influence of different coil positions and orientations on
194 the determination of the effective stimulation site. In addition to M1 and P, two more coil
195 positions were included, shown in Fig. 2(b), 2 cm inferior and 2 cm superior to M1,
196 respectively. For each position, the number of coil orientations was increased to 5 (-90°, -45°,
197 0°, 45°, 90°) with respect to $M1_{45°}$, resulting in 20 experimental conditions. The coil
198 positions/orientations were recorded by the neuronavigation system and assigned to the
199 respective MEPs. The lower surface of the coil was lying on the scalp to minimize the coil-scalp
200 distance.

For each of these conditions, single biphasic pulses with an inter stimulus interval of 4 s were applied. The MEPs were lowpass filtered with a 6th order Butterworth filter with a cutoff frequency of 500 Hz. Afterwards, the peak-to-peak amplitudes of the MEPs were in a time window of 18 to 35 ms after the TMS pulse. An example MEP is shown in Fig. 3(a). Stimulation intensities were chosen to sample the complete I/O curve for each experimental condition, unless maximal stimulator output was reached before (Fig. 3(b)). Intensity was increased in steps of 2% stimulator output, and in parts where the I/O curve had a high gradient in steps of 1% (Bungert et al., 2017, supplemental material). For each intensity, 5-10 stimulations were performed to determine an average MEP amplitude. An outlier correction was performed and MEPs were omitted from the analysis, which were recorded with deviations in coil position of ±3 mm and orientation of ±5° with respect to every axes. A typical set of data points is shown in Fig. 3(b) (blue dots). Thereafter, a sigmoidal function was fitted in a least-square sense:

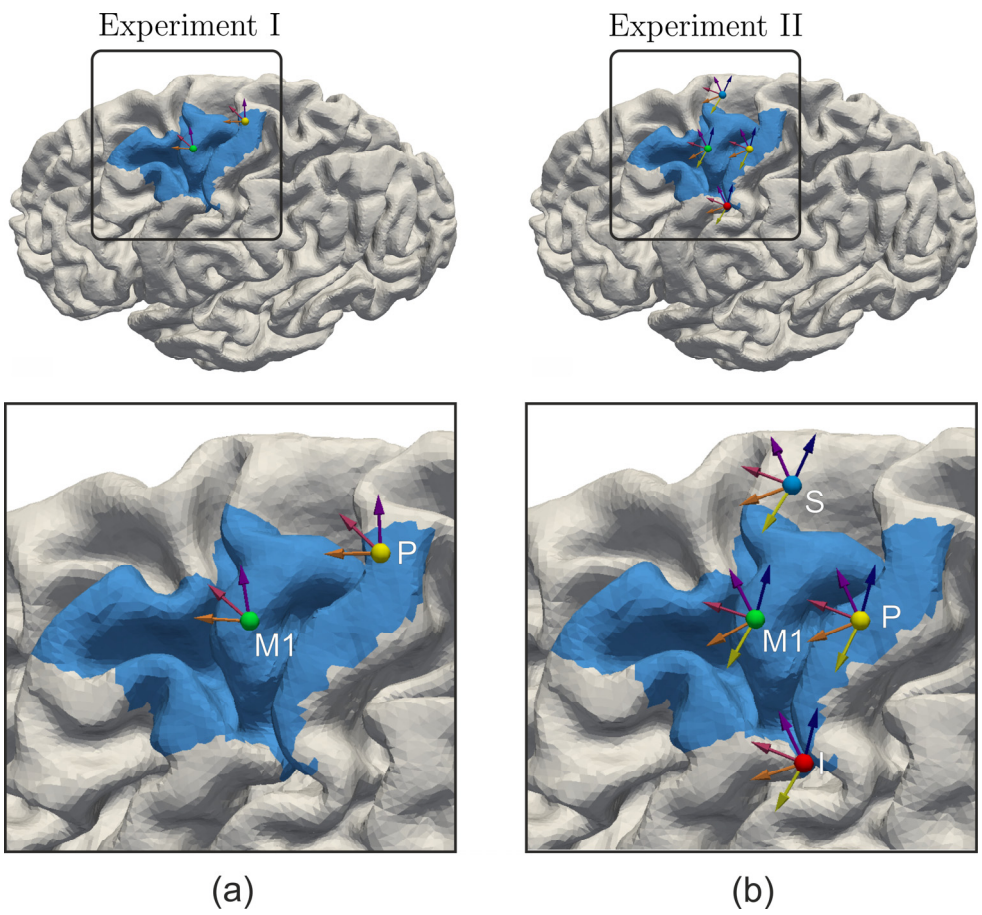

Figure 2: Coil positions and orientations used in (a) Experiment I and (b) Experiment II. The locations are exemplarily shown for subject S8. The number of experimental conditions increases from six to 20. The blue area is the region of interest, comprised of the somatosensory cortex S (BA 1, BA 3), M1 (BA 4), and the dorsal part of the premotor cortex (BA 6).

$$s_i(x) = \frac{a_i}{1 + e^{-b_i(x - x_{0,i})}} \quad (1)$$

where a_i is the saturation amplitude, b_i the slope, and $x_{0,i}$ is the location of the turning point on the abscissa. If only a part of the I/O curve could be determined experimentally, a sigmoidal function cannot be reliably fitted and an exponential or linear function is used instead. The selection of the optimal model was performed using the Akaike information criterion (AIC, Akaike, 1974).

The procedure was repeated for all experimental conditions, that is, for different coil positions and orientations. The sequence of the conditions was pseudo-randomized and the coil position and orientation were recorded for each individual stimulation.

2.2 Numerical simulations of the induced electric field

The calculations of the electric field were conducted with SimNIBS v2.0 (Thielscher et al., 2015) using high-resolution anisotropic finite element models (FEMs), as exemplary shown for one subjects in Fig. 4. The individual head models were generated from MRI data using the pipeline described in Windhoff et al. (2013), employing FreeSurfer (http://surfer.nmr.mgh.harvard.edu/, Dale et al., 1999; Fischl et al., 1999) and FSL (https://fsl.fmrib.ox.ac.uk/fsl/fslwiki/FSL, Woolrich et al., 2009; Smith et al., 2004; Jenkinson

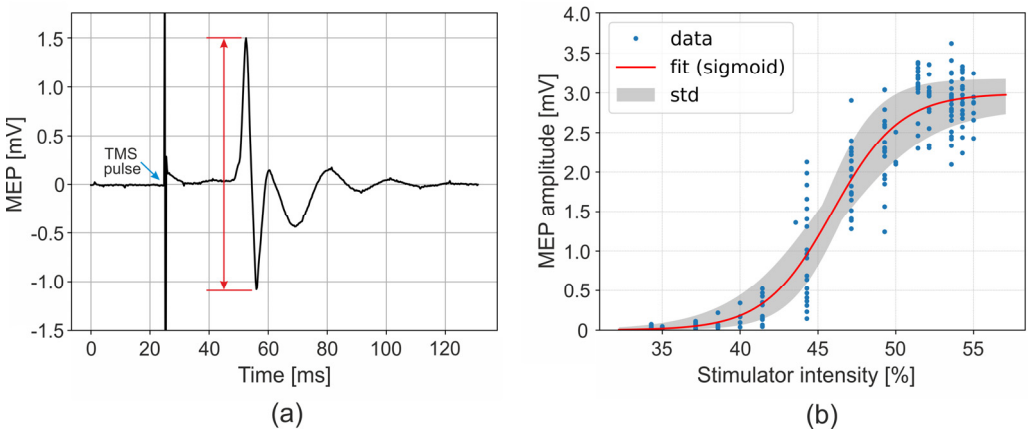

Figure 3: (a) Measured motor evoked potential (MEP) showing the stimulation artifact (blue arrow) and highlighting the peak-to-peak amplitude (red arrow). (b) I/O curve characterizing the MEP amplitudes as function of the stimulator intensity for one particular experimental condition. The blue dots are the MEP amplitudes for the different stimulator intensities. The red curve is the fitted analytical function. Depending on the best Akaike information criterion (AIC), the MEP amplitudes are fitted to sigmoidal, exponential or linear functions (here: sigmoid). The black lines are possible I/O curves resulting from the uncertainty in the experimental data.

et al., 2012). The head models are composed of ~$1.3 \cdot 10^6$ nodes and ~$7 \cdot 10^6$ tetrahedra. T1 and T2 images were used for segmenting the main tissues of the head: scalp, skull, grey matter (GM), white matter (WM), and cerebro-spinal fluid (CSF). Diffusion weighted images were used to reconstruct the conductivity tensors in the WM using the volume normalized mapping approach (Güllmar et al., 2010). The structural images were acquired with a 3 Tesla MRI scanner (Siemens Verio or Skyra) and a 32 channel head coil. The following images were acquired: (i) T1-weighted: MPRAGE with 176 sagittal slices, matrix size = 256 x 240, voxel size = 1 x 1 x 1mm³, flip angle 9°, TR/TE/TI = 2300/2.98/900ms (Repetition, Spin echo, Inversion Time), (ii) T2-weighted: 192 sagittal slices, matrix size = 256 x 258, voxel size = 0.488 x .488 x 1mm³, flip angle 120° TR/TE = 5000/395ms (iii) diffusion MRI (67 axial slices, matrix size 128 x 128, voxel size 1.71875 x 1.71875 x 1.7mm³, TE/TR 80/7000ms, flip angle 90°, 67 diffusion directions, b-value 1000s/mm³. An additional b0 image with reversed encoding direction was recorded for distortion correction with FSL topup and eddy. The T1 image was also used for neuronavigation during TMS. If adequate scans (age less than 1 year)

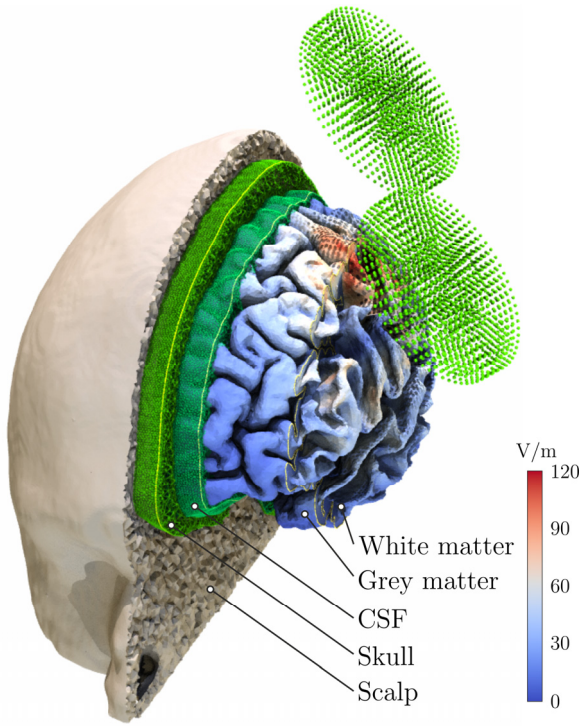

Figure 4: Example of the realistic anisotropic head model of one subject, which is used for the numerical simulations of the induced electric field. The model consists of $1.26 \cdot 10^6$ nodes and $7.12 \cdot 10^6$ tetrahedra. The TMS coil is modeled using 4440 magnetic dipoles (green dots) with optimized dipole moments located in five layers. The grey matter surface is color coded with the magnitude of the induced electric field.

already existed for the subjects in the image database, these scans were utilized.

All TMS coils were individually modelled by magnetic dipoles based on X-ray images. Coil wiring differences (shifts of several millimeters and tiltings of about 2-5°) were observed and accounted for. Each coil model consists of ~4500 magnetic dipoles. These dipole models were compared to a detailed current density based FEM model using Comsol Multiphysics v4.4 (COMSOL, Inc., Burlington, MA, USA) and yielded magnetic field errors of < 0.1% at a distance of 15 mm.

The magnetic field produced by the coil is calculated in advance in terms of the magnetic vector potential $\mathbf{A}$. The primary electric field is then given by $\mathbf{E}_p = -j\omega\mathbf{A}$, where $\omega = 2\pi f$ is the angular frequency of the biphasic TMS pulse. The electric potential ϕ in the nodes is calculated by solving the Laplace equation $\nabla \cdot ([\boldsymbol{\sigma}]\nabla\phi) = 0$, considering anisotropic conductivity tensors $[\boldsymbol{\sigma}]$ inside each element together with the boundary conditions given by the law of current conservation $\nabla \cdot \mathbf{J} = 0$. After calculating the secondary electric field $\mathbf{E}_s = -\nabla\phi$, the total induced electric field is given by $\mathbf{E} = -j\omega\mathbf{A} - \nabla\phi$. The conductivity values for the five examined tissues ($\sigma_{Scalp} = 0.465$ S/m, $\sigma_{Skull} = 0.01$ S/m, $\sigma_{GM} = 0.275$ S/m, $\sigma_{WM} = 0.126$ S/m, $\sigma_{CSF} = 1.654$ S/m) were taken from Thielscher et al. (2011) and Wagner et al. (2004). A more detailed description about the FEM solver is given in Windhoff et al. 2013 and its supplemental material.

A region of interest (ROI) was defined covering the somatosensory cortex S (BA 1, BA 3), M1 (BA 4), and the dorsal part of the premotor cortex (BA 6) with Freesurfer and a mask was created for the Freesurfer average template and mapped to each individual subject.

The following analyses were performed on the midlayer between the outer surfaces of the GM and WM compartments in order to avoid boundary effects of the electric field due to conductivity discontinuities. The electric field was interpolated in the nodes of this surface in a post-processing step. Fig. 5 shows the magnitude $|\mathbf{E}|$, the normal component $|\mathbf{E}_\perp|$ and the tangential component $|\mathbf{E}_{||}|$ of the electric field at the midlayer surface for three different coil positions and orientations in one exemplary subject. One can readily identify the different electric field distributions in the highlighted ROI for the different experimental conditions.

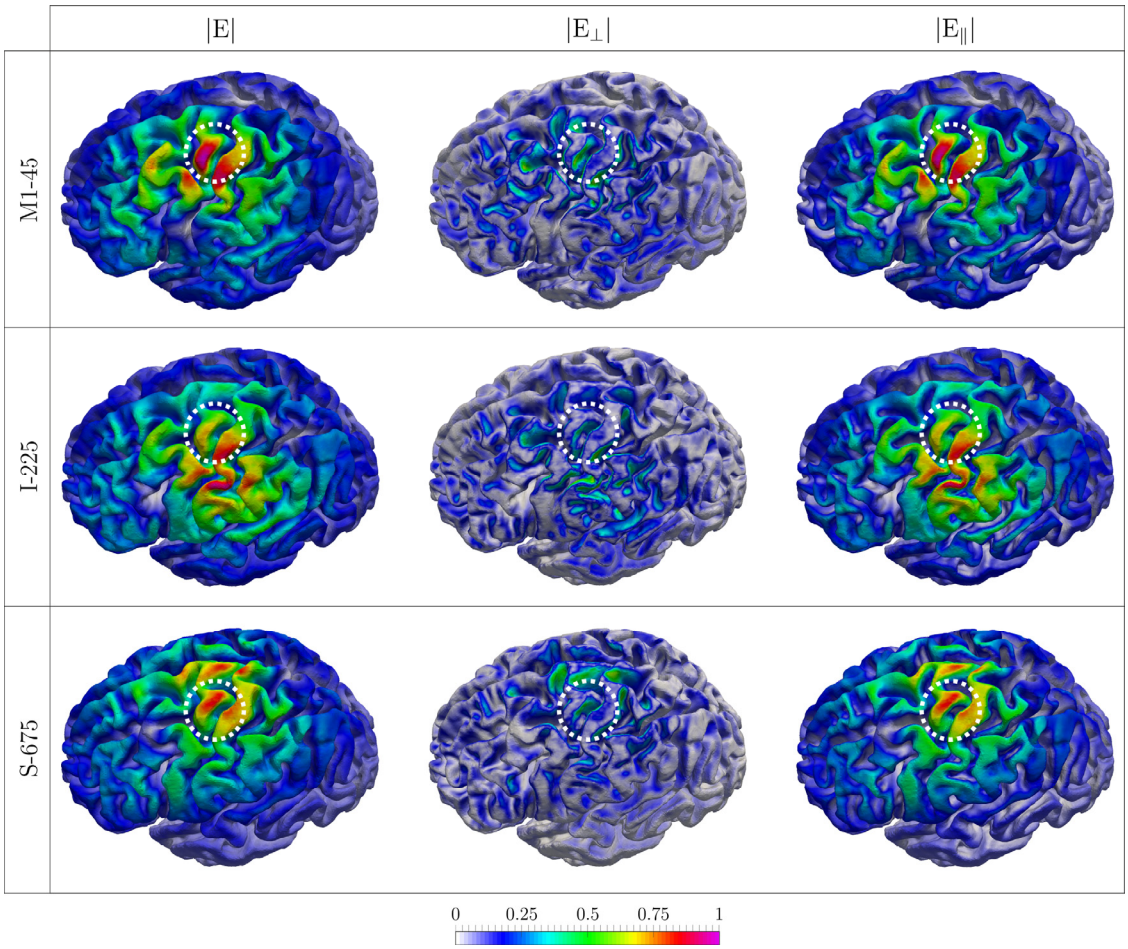

Figure 5: Three electric field distributions, i.e. the magnitude of the electric field $|\boldsymbol{E}|$, the normal component $|\boldsymbol{E}_{\perp}|$, and the tangential component $|\boldsymbol{E}_{||}|$ for one exemplary subject. The electric field is normalized to allow comparability between the different experimental conditions. The white circle highlights the hand knob area in M1 (region of interest).

2.3 Determining the site of stimulation

The core concept of the proposed method is illustrated in Fig. 6. We assume that at the site of activation the correlate between electric field and MEP is stable, i.e. the same electric field evokes the same behavioral output independent on the location or orientation of the TMS coil it was generated with. Exploiting this property, we can single out the site of stimulation by calculating *cortical I/O curves* that represent the relationship between the electric field in the cortex and the resulting MEP, and then comparing the cortical I/O curves of the different experimental conditions. Only at the true cortical site of stimulation, the I/O curves of all conditions should be highly similar to each other. Practically, this is done by transforming the measured I/O curve for each condition (representing the relationship between stimulation intensity in percent of maximal stimulator output, %MSO, and MEP amplitude) to E-MEP-curves (representing the relationship between the electric field at a particular cortex location

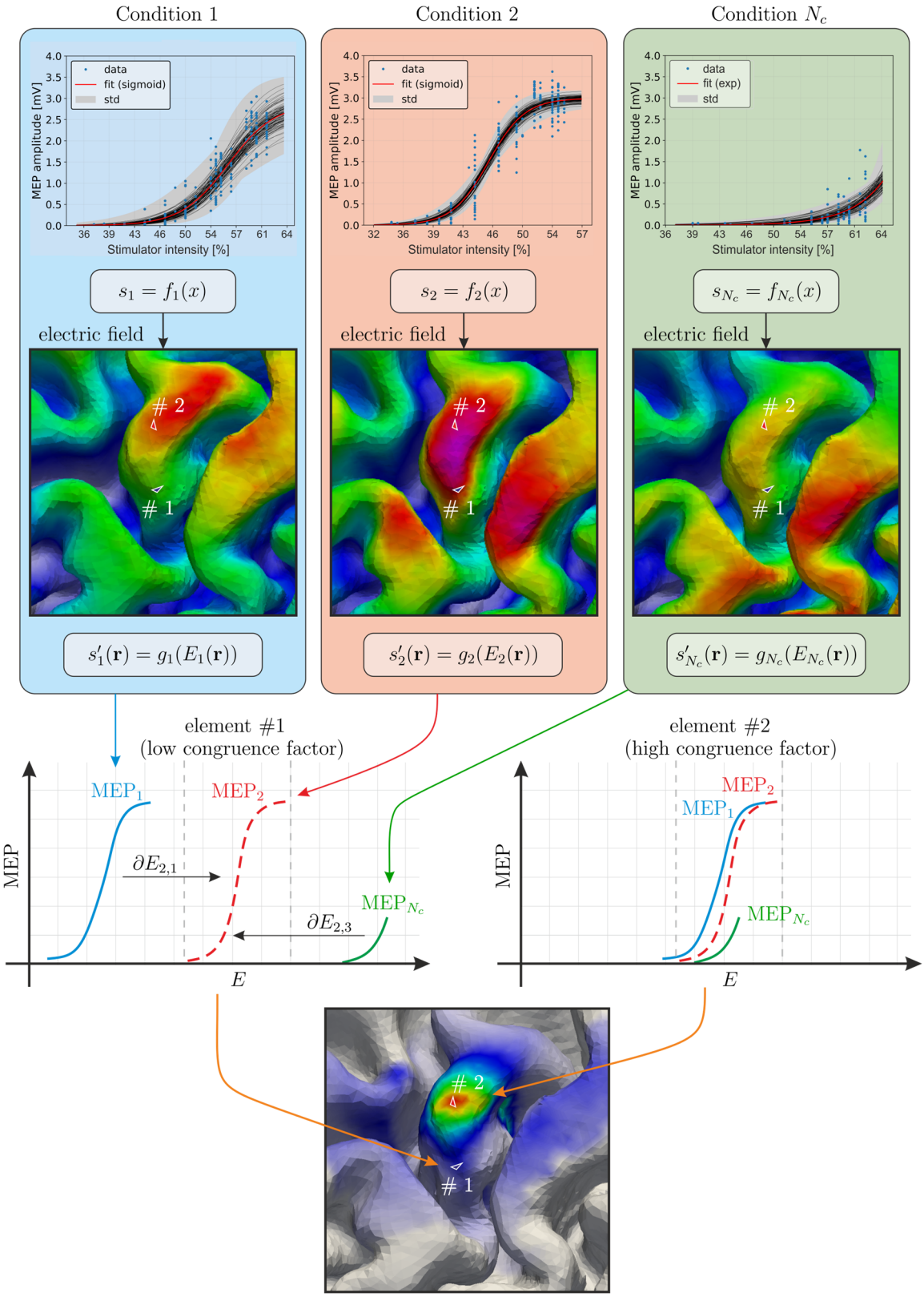

Figure 6: Principled approach to determine the site of stimulation during TMS. The congruence factor is based on the assumption that the electric field, which is causal to the observed behavioral effect, agrees between the experimental conditions. The measured I/O curves are transformed to element wise E-MEP-curves using electromagnetic field modeling (see text). The congruence factor between the E-MEP-curves inversely depends on the amount of transformation (shift) necessary to obtain maximum overlap between the E-MEP-curves in each element.

and the respective MEP amplitude). The electric field distribution throughout the brain can be computed as a function of the stimulation intensity using the numerical techniques described above, thereby taking 100% MSO as corresponding to a maximal change of the coil current of 140 A/μs for the used stimulator-coil combination. Due to the linear relationship between electric field strength and stimulator intensity, the E-MEP curves are shifted and horizontally scaled versions of the measured I/O curve, with different shift and scale parameters in each position. Hence, the function types of each I/O curve and their corresponding E-MEP curves are the same (i.e. sigmoidal, exponential, or linear). E-MEP curves can be determined for all different components of the electric field vector ($|\mathbf{E}|$, $|\mathbf{E}_{\perp}|$, $|\mathbf{E}_{||}|$) or, in principle, any other derived quantities thereof. This approach allows to compute a position-wise *congruence factor* $c(\boldsymbol{r})$, which quantifies the similarity between the E-MEP curves from the different experimental conditions.

The agreement between different I/O curves is quantified by computing the inverse variance of the optimal shifts τ_i with $i = 1 \dots N_c$ of the N_c I/O curves across the experimental conditions.

$$c(\boldsymbol{r}) = \left(\frac{1}{N_c} \sum_{i=1}^{N_c} \frac{\left(\bar{\tau}(\boldsymbol{r}) - \tau_i(\boldsymbol{r})\right)^2}{\bar{E}^2(\boldsymbol{r})} \right)^{-1} \tag{1}$$

The congruence factor $c(\boldsymbol{r})$ is calculated in each element in the ROI on the cortex by determining the inverted variance of the τ_i, additionally weighted by the squared average electric field $\bar{E}^2(\boldsymbol{r})$ at this location. Hence, the congruence factor quantifies a relative similarity between the observations in the different experimental conditions independent on the scale of the electric field. The more similar the curves are, the higher is the inverse variance. The optimal shifts τ_i are obtained by determining the individual locations where the overlap against a reference, e.g. the first E-MEP curve, is maximized. As a result, the problem of determining the congruence factor turns into many optimization problems to calculate the shifts τ_i for each condition and in each element in the ROI:

$$\min_{\tau_i} \left\| s'_{REF}\big(E(\boldsymbol{r})\big) - s'_i(E(\boldsymbol{r}) - \tau_i) \right\|_2 \tag{2}$$

Where s'_{REF} and s' denote the reference and one of the I/O curves the shift is calculated for, respectively. This method is computationally expensive but very general, as it is independent of the involved function types. This is advantageous because it is often the case that the experimentally determined I/O curves do not capture the whole range of the relationship between electric field and MEP amplitude involving different functions to describe them (exponential or linear, see above). If, however, each E-MEP curve can be represented as analytical sigmoidal function, parameterized by its turning point $x_{0,i}$, the shifts τ_i are directly given by $\tau_i = x_{0,i} E_i(\boldsymbol{r})$ and the computational expensive optimization from (2) can be avoided, thus making the method computationally very efficient. This approach is advantageous in terms of computational cost and is preferred in the current study if all I/O curves are represented by sigmoidal functions.

As the standard Freesurfer average template (fsaverage) suffers from several malformed elements at the primary motor cortex with each of roughly the 20-fold size as the average element, we created a group-based average with Freesurfer. In this iterative procedure, a randomly chosen subject was first used as initial template and all subjects were registered to this template. In the second step, the template was updated based on these registrations. The third step comprised the registration of all subjects to this new template. The second and third steps were then repeated to improve the template. The final subject registrations were used for mappings between individual subjects and the final group average.

2.4 Uncertainty and sensitivity analysis

The congruence factor is influenced by several parameters. For example, previous studies have shown that, because of their large uncertainties, the electrical ohmic conductivities of brain tissues have a strong influence on the magnitude of the electric field (Weise et al., 2015; Codecasa et al., 2016). Furthermore, the estimated parameters of the fitted MEP curves are also uncertain due to measurement noise (Fig. 3(b) grey interval). Therefore, uncertainty and sensitivity analyses are important to investigate the stability of the results and identify the parameters and their combinations with the largest impact on the results.

Since the problem is computationally complex and features a large number of parameters $\boldsymbol{p}$, an efficient approach is necessary to conduct the analysis. Here, we applied the generalized

polynomial chaos (gPC) method (Ghanem et al., 2016). Its mathematical background is described in detail in Section 1.3 of the *Supplemental Material*. In short, the gPC is based on the construction of a polynomial surrogate of the congruence factor depending on the uncertain model parameters and their associated probability density functions.

Since the electric field depends on the electrical conductivities $[\boldsymbol{\sigma}]$ of the brain tissues, the congruence factor will be influenced as well. The conductivities of GM, WM and CSF were modelled as beta distributed random variables. The impact of the other tissues, like skull and scalp on the electric field was shown to be negligible in previous studies (Weise et al., 2015; Codecasa et al., 2016; Bicalho et al., 2018). However, extending previous studies, the impact of the level of conductivity anisotropy was included. The conductivity tensor $[\boldsymbol{\sigma}]$ for each voxel is derived from the diffusion tensor using the volume normalize approach (Güllmar et al., 2010). This tensor can be visualized as ellipsoid (*Supplemental Material*, Fig. S1). A spherical ellipsoid represents isotropic conductivity with equal conductivity in each direction, while a cigar shaped tensor indicates that the conductivity is much larger in one direction. We introduce an anisotropy factor α that transforms the diffusion tensor from the isotropic case ($\alpha = 0$) via the original tensor obtained from DTI ($\alpha = 0.5$) to a very anisotropic case ($\alpha = 1$). Although, in principle, α could be different in each voxel, this would render the resulting problem intractable. Instead, we assume that α is the same for all voxels. This reflects systematic errors and uncertainties in the transformation between the diffusion tensor, which depends on the mobility of water molecules, and the conductivity tensor, which represents the mobility of charges. A detailed mathematical description of the parametrization of the fractional anisotropy is given in *Supplemental Material: Section 1.2*.

In addition to the conductivity and anisotropy uncertainties, the turning points $x_{0,i}$ from the sigmoidal I/O curves are included in the uncertainty analysis. Their uncertainties are derived from the confidence intervals of the curve fits (cf. Fig. 3(b)). The stochastic properties of all investigated parameters are summarized in Table 1. The model of the congruence factor used in the gPC based uncertainty and sensitivity analysis is described in detail in *Supplemental Material: Section 1.4*.

After deriving the polynomial surrogate using the gPC, the spatial distribution of the expectation $\mu(\boldsymbol{r})$ and the variance $\nu(\boldsymbol{r})$ of the congruence factors $c(\boldsymbol{r})$ can be calculated. We further analyzed the relative standard deviation $RSD = \sqrt{\nu(\boldsymbol{r})}/\mu(\boldsymbol{r})$ to identify possible regions, where the congruence factor is primarily influenced. Finally, in the sensitivity analysis, the variance is decomposed into its origins by a Sobol decomposition. The Sobol indices $S_i(\boldsymbol{r})$ represent portions of the total variance $\nu(\boldsymbol{r})$, which are due to individual parameters p_i or a combination thereof, e.g. the conductivity of GM or the combination between different measurement parameters (Sobol, 2001; Sudret, 2008).

Table 1: *Limits and shape parameters of the model parameters for subject S1*

Parameter	Description	Min	Max	p / q	Reference / source
$\boldsymbol{\sigma_{WM}}$	White matter (WM)	0.1 S/m	0.4 S/m	3 / 3	Li et al. (1968) Nicholson (1965) Akhtari (2010)
$\boldsymbol{\sigma_{GM}}$	Grey matter (GM)	0.1 S/m	0.6 S/m	3 / 3	Li et al. (1968) Ranck (1963) Logothetis et al. (2007) Yedlin et al. (1974)
$\boldsymbol{\sigma_{CSF}}$	Cerebrospinal fluid (CSF)	1.2 S/m	1.8 S/m	3 / 3	Gabriel et al. (2009) Baumann et al. (1997)
$\boldsymbol{\alpha}$	Anisotropy scaling	0.4	0.6	3 / 3	Tuch et al. 2001
$\boldsymbol{x_{0,S(90°)}}$*	MEP curve	145.9 [A/µs]	185.9 [A/µs]	4 / 4	experiment
$\boldsymbol{x_{0,S(135°)}}$*	——"——	150.0 [A/µs]	190.0 [A/µs]	4 / 4	——"——
$\boldsymbol{x_{0,I(45°)}}$	——"——	80.7 [A/µs]	87.9 [A/µs]	4 / 4	——"——
$\boldsymbol{x_{0,I(135°)}}$	——"——	125.7 [A/µs]	145.7 [A/µs]	4 / 4	——"——
$\boldsymbol{x_{0,P(0°)}}$	——"——	124.2 [A/µs]	133.3 [A/µs]	4 / 4	——"——
$\boldsymbol{x_{0,M1(90°)}}$	——"——	86.0 [A/µs]	98.7 [A/µs]	4 / 4	——"——

Note: These parameters were considered in the uncertainty and sensitivity analysis to determine the site of stimulation by means of the congruence factor. The star marks conditions, where only the lower tail of the I/O curve could be determined. These curves are subject to a higher measurement uncertainty.

3 RESULTS

In the following, we present the results from Experiment I (15 subjects and 6 experimental conditions) and Experiment II (3 subjects and 20 experimental conditions). The latter includes a permutation analysis to determine the number of stimulation sites and corresponding coil positions required to determine the stimulation site reliably. The results from both studies are then compared. Finally, the results of the uncertainty and sensitivity analysis of the congruence factor are presented for one exemplary subject. The most influencing parameters of the numerical model and the experimental data are identified in the ensuing sensitivity analysis.

3.1 Experiment I (15 subjects, 6 experimental conditions)

The congruence factors of the group average are shown in Fig. 7(a) and for all 15 subjects individually in Fig. 7(b). The electric field distributions of all conditions were determined for each subject and combined with the fitted MEP curves using the *optimal curve shift approach* because not all MEP curves could be fitted to sigmoidal functions. In 6/15 subjects, which are marked with a star (*), no evaluable I/O curve could be determined in case of the posterior coil position $P_{0°}$. Hence, the congruence factor is determined using only 5 of the 6 conditions. The congruence factor was calculated for the magnitude ($|\mathbf{E}|$), as well as the normal ($|\mathbf{E}_{\perp}|$) and the tangential ($|\mathbf{E}_{||}|$) component of the induced electric field. The magnitude and the tangential component reach substantially higher congruence factors and smoother spatial distributions than the normal component $c(|\boldsymbol{E}_{\perp}|)$. In general, a clear hotspot for $c(|\boldsymbol{E}|)$ and $c(|\boldsymbol{E}_{||}|)$ could be identified in the hand knob area of M1 on the gyral crown of the average template. However, considering the individual congruence factor maps shows that in 7/15 subjects (S1-S7, highlighted in Fig. 7 with a green background) we find clear and unique hotspots only on the gyral crowns in the hand knob area. In 4/15 subjects (S8-S11, Fig. 7, yellow background), we observe, besides the hotspot in M1, a second hotspot in the somatosensory cortex (S). In 4/15 subjects (S12-S15, Fig. 7, orange background), we found only a dominant hotspot in S. We hypothesize that this is due to array ambiguities, i.e. spurious overlaps, of the realized electric fields and the missing I/O curve of condition $P_{0°}$, in 2/4 and 3/4 subjects of the two groups, respectively. Note that maximum values of the congruence factors substantially differ across

subject. This is because small differences in near zero variances among I/O curves may result in large difference in their inverse, that is the associated congruence factors.

We expected that additional experimental conditions, i.e. more coil positions and orientations, would improve the results of the congruence factor towards more plausible hotspot locations in the M1 hand knob area. This hypothesis was investigated in Experiment II by increasing the number of coil positions and orientations from 6 (resp. 5) to 20 (cf. Fig. 2(b)). For that experiment we selected one subject out of each of the three result groups described above: S1, S8, and S12.

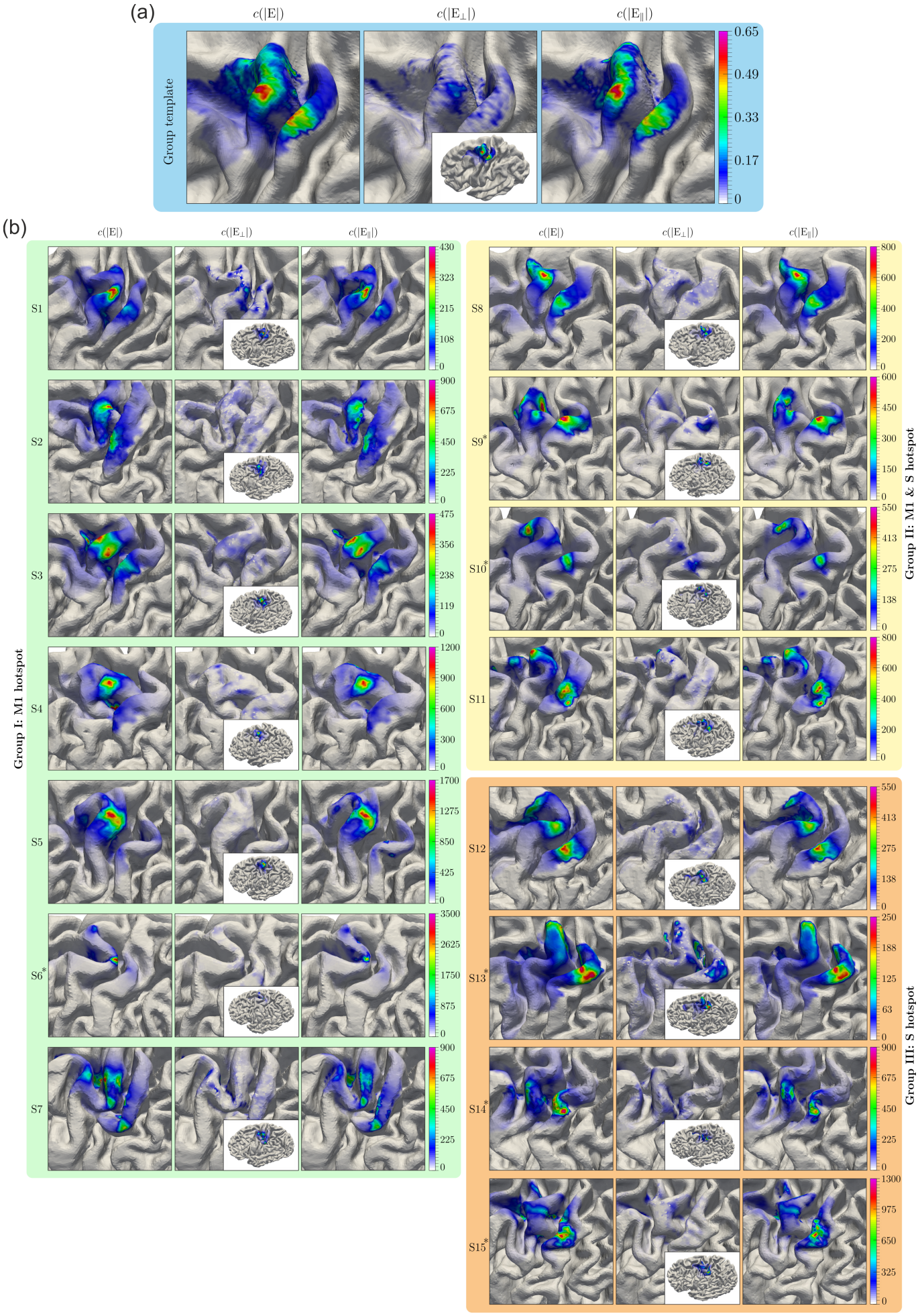
(a)
c(|E|)
c(|E⊥|)
c(|E∥|)
Group template
0.65
0.49
0.33
0.17
0
(b)
Group I: M1 hotspot
S1
S2
S3
S4
S5
S6*
S7
Group II: M1 & S hotspot
S8
S9*
S10*
S11
Group III: S hotspot
S12
S13*
S14*
S15*

410

Figure 7: Congruence factor maps of 15 investigated subjects considering six experimental conditions (Experiment I). The congruence factors are calculated for the magnitude, the normal and the tangential component of the electric field using the optimal curve shift approach. 7/15 subjects show unique hotspots in M1 (highlighted in green); 4/15 subjects show hotspots in M1 and S (highlighted in yellow) and 4/15 subjects show hotspots in S only (highlighted in orange); The stars (*) mark subjects, where no evaluable MEPs could be determined in case of the posterior coil position $P_{0°}$. In these cases, the congruence factor is determined using only five conditions; All results are normalized, mapped and superimposed on the group average template shown on the top (highlighted in blue).

3.2 Experiment II (3 subjects, 20 experimental conditions)

This experiment was conducted with an extended set of coil positions and orientations as shown in Fig. 2(b). For each subject, 20 electric field distributions were calculated and combined with the obtained MEP curves to determine the congruence factor maps. In this experiment, all I/O curves could be fitted to sigmoidal functions, which permits to avoid the computationally expensive optimizations step from (2) by directly using the variance of the turning points.

Because 20 experimental conditions are too time consuming to record in future mapping applications based on the proposed method, we investigated how the congruence factor convergences depending on the number of experimental conditions. This enabled us to determine an optimal number and selection of coil positions/orientations, in order to reduce the experimental effort. Thus, for each subject, a permutation study was performed by determining the congruence factor for all combinations of $k = 2 \dots 20$ available experimental conditions. The total number of considered conditions is $\sum_{k=2}^{20} \binom{20}{k} = 1{,}048{,}555$. We quantified the focality of each congruence factor map by determining the area with $c > 30$. This value was chosen based on the permutation results data to allow comparability between the combinations and subjects. The smaller this area, the more concentrated the map is. That is, the more uniquely the causal relationship between electric field and MEP could be determined.

The results of the permutation study are shown in Fig. 8 for one exemplary subject (S1). The results for the remaining subjects are very similar and shown in *Supplemental Material* Fig. S3 and Fig. S4, respectively. We expected that a lower cross-correlation across the condition-wise electric fields would allow for a higher discriminative power in the determination of the stimulation site. This tendency is confirmed by the analysis in Fig. 8(a), showing a correlation

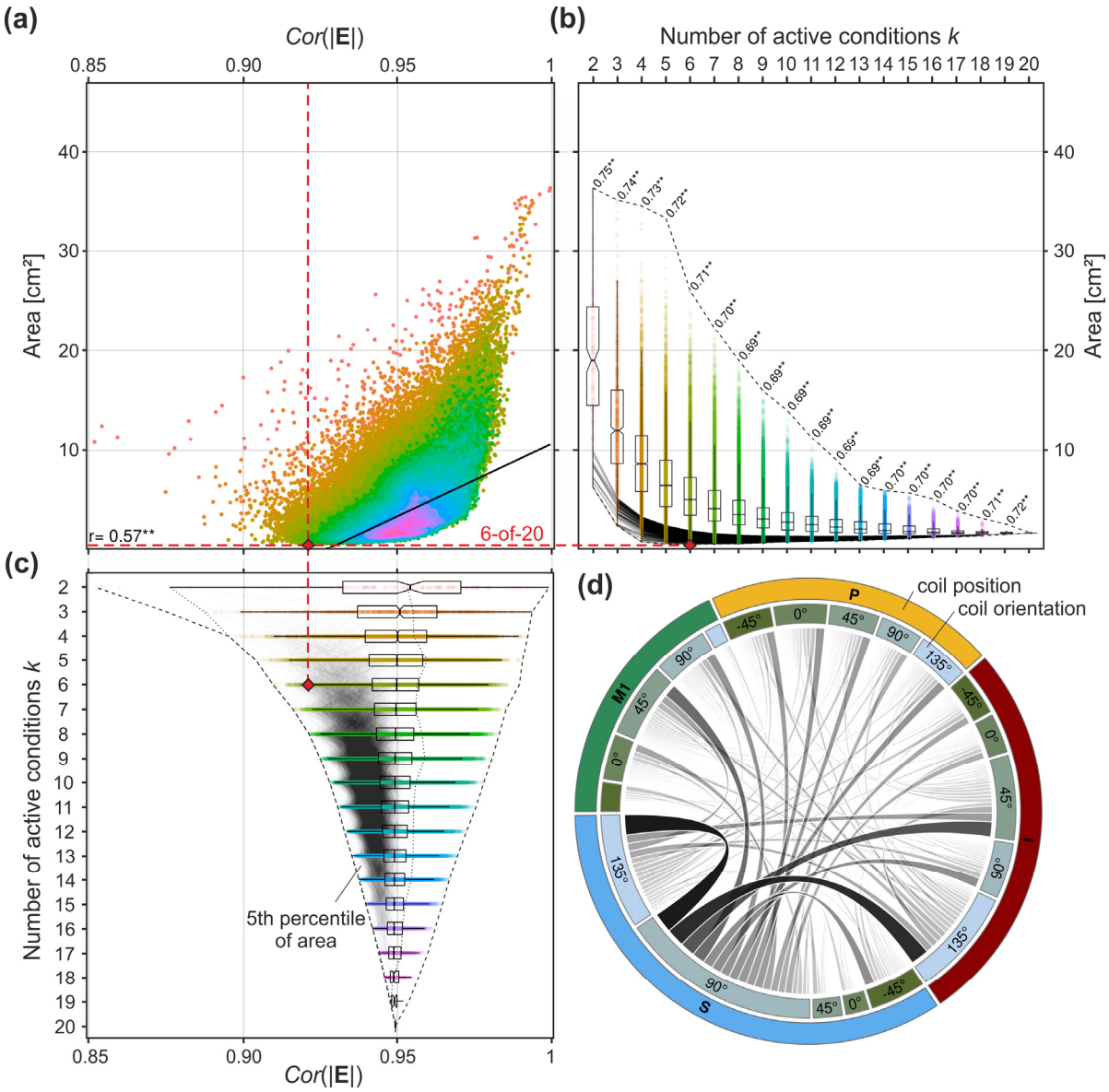

Figure 8: Permutation analysis interrelating the cross-correlation of the electrical fields from the different experimental conditions of Experiment II for subject S1 with the corresponding hotspot area. The hotspot area is defined as the region where $c > 30$. For each case k, the congruence factor is determined $\binom{20}{k}$ times. (a) Relationship between the cross-correlation of the electric field magnitude and the resulting hotspot area size. Colors: active conditions k. The correlation coefficient between the hotspot size and the cross-correlation of the electric fields over all k (black line) is $r = 0.57$ ($p \ll .001$). (b) Boxplot of the hotspot area of the congruence factor in dependence of the number of active conditions k. Box areas indicate the 25% to 75% quantiles with notch at median. Correlation coefficients between the hotspot size and the cross-correlation of the electric fields for each *k* are given. ** depict $p < .01$ (after Bonferroni correction). Grey lines: 5th percentile of the best condition combinations for each *k* (same as in (c)). Dashed lines: absolute range. The variation of the hotspot area size decreases with increasing k. (c) Relationship between the cross-correlation coefficient of the electric fields and the number of active conditions k. Box areas indicate the 25% to 75% quantiles with notch at median. Grey lines: 5th percentile of the best condition combinations for each *k* (same as in (b)). Dashed lines: absolute range. The dashed red lines highlight the case of the 6 coil positions and orientations, where the congruence factor map was most focal. Its cross-correlation coefficient is with 0.921 lower than the first quartile of possible solutions. (d) Chord graph highlighting the interaction and relative contribution between different coil positions (outer circle) and coil orientations (inner circle) from the 5th percentile of best condition combinations over all *k* resulting in small hotspot areas (highlighted with black lines in (b)).

of $r = 0.57$ $(p \ll .001)$ between the size of the hotspot area and the cross-correlation of the electric fields over all k. Looking at the individual number of conditions k, we observed that the correlation between the resulting hotspot area and the cross-correlation of the electric fields is even more apparent for low k (Fig. 8(b), correlation coefficients). The median of the hotspot area converges when increasing the number of active conditions. Moreover, the spread of the area decreases by adding more information to the congruence factor calculation. Importantly, the smallest areas (lower dashed line in Fig. 8(b)) indicate that there exist condition combinations for $k \geq 5$, which result in similar or even smaller areas as for $k = 20$. This indicates that it is possible to determine the site of stimulation with relatively few measurements by selecting optimal coil positions and orientations.

The relationship between the cross-correlation of the electric fields and the number of active conditions k is shown in Fig. 8(c). The cases resulting in the smallest 5th percentile of the hotspot area are shown as thin lines in the shaded area, corresponding to the ones in Fig. 8(b). As expected, these cases are concentrated in regions of low cross-correlation.

In Fig. 8(d), the data was further analyzed regarding to which combinations of experimental conditions are especially informative and allow for very focal hotspots. The analysis is performed for $k = 6$. The appearance of each condition and its co-occurrence with other conditions is accumulated over all condition combinations, which are part of the smallest 5th percentile of the hotspot area (grey shaded area in Fig. 8(b)). We observed that the co-occurrence is not random and combinations surrounding M1, i.e. inferior, superior, and posterior, appear more often than coil positions over M1 itself. The corresponding coil orientations considerably differ from each other and connections between $S_{90°}$, $S_{135°}$, $I_{45°}$, and $I_{135°}$ stand out. Moreover, it can be observed that posterior conditions occur frequently in combination with $S_{90°}$, which further confirms the former hypothesis regarding the need for highly varying electric field distributions. This behavior is pronounced even stronger for subjects S8 and S12 shown in Fig. S3 and Fig. S4 in the *Supplemental Material*.

In the following, the results for $k = 6$ condition combinations out of the 20 experiments (6-of-20) resulting in the smallest hotspot area are described in more detail and compared to Experiment I as well as to the full 20-of-20 result. The results are shown in Fig. 9 for each

subject. The congruence factor maps were normalized with respect to their individual maxima to allow comparability. For subject S1, we already found a unique hotspot in the M1 hand knob area in Experiment I. The results of Experiment II show that this pattern is reproducible and even more focused (as the deflection on the somatosensory cortex is weaker) for the best combination of 6-of-20 conditions. Hence, for this subject, the coil positions of Experiment I were already sufficient to determine the site of stimulation in plausible manner. The second subject belongs to the group, which showed hotspots in both M1 and S (Experiment I). In Experiment II, a single hotspot is limited to the M1 region as well, and the deflection in S disappeared. The M1 hotspot is also slightly shifted inferior. The third subject belongs to the group, which showed a hotspot only in S in Experiment I. In Experiment II, however, the hotspot moved to M1 supporting our previous hypothesis of insufficient information content concerning the combination of electric field profiles and measured MEP amplitude curves due to a limited classification ability of the electric fields. As indicated by the convergence results of the permutation study (Fig. 8(a)), adding the remaining conditions of Experiment II (20-of-20 case) does not yield any improvement for any of the three subject groups.

For subject S1 (first row in Fig. 9), the cross-correlation of the electric field distributions in the ROI of Experiment I was 0.951, and that of Experiment II 0.921. For subject S8 (second row in Fig. 9) the cross-correlation was 0.953 and 0.925 for Experiment I and II, respectively. It can be observed that the use of less correlating electric field distributions did increase the quality of the reconstruction. Finally, for subject S12 (third row in Fig. 9) the cross-correlations were nearly the same with 0.951 and 0.953 from Experiment I to II, respectively. However, the improvement of the results indicates that the selected coil positions and orientations in Experiment II are more suitable to determine the congruence factor, such that the distinguishability between the cortical positions is higher than in Experiment I. It is emphasized that this property is only partly reflected by the cross-correlation coefficient. A definition of a more sophisticated ambiguity measure to determine an optimal set of coil positions and orientations will be the subject of a future study.

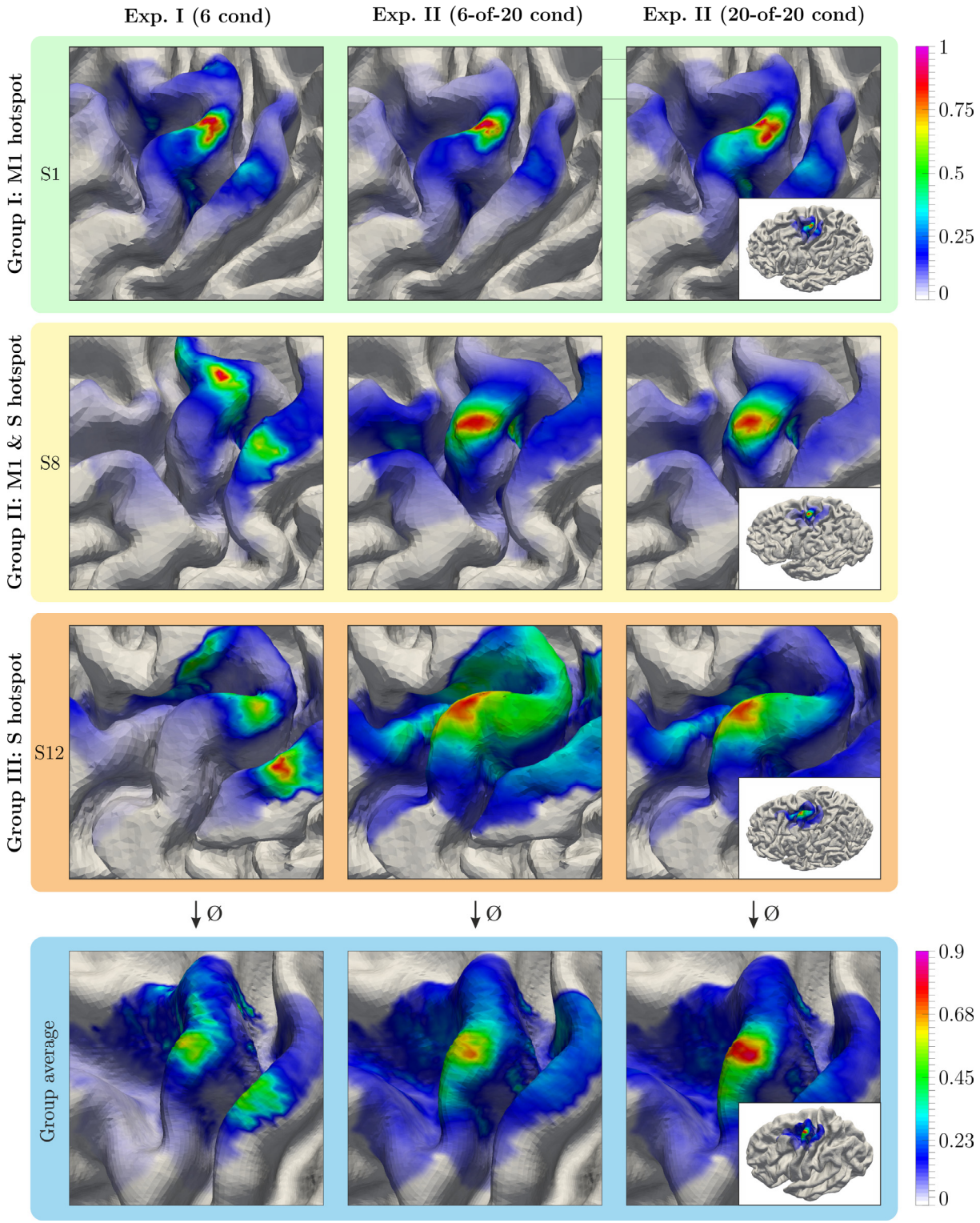

Figure 9: Normalized congruence factor maps of 3 subjects. The first column shows the results of Experiment I with 6 experimental conditions; the middle row depicts the 6-of-20 condition combination with the smallest hotspot area from Experiment II; The right column shows the congruence factor maps when all 20 experimental conditions of study II are taken into account in the analysis. The subjects were chosen such that one of each of the result groups in study I (M1 only, M1 and S, S only, see Fig. 7) was included.

3.3 Uncertainty and sensitivity analysis

We further analyzed the congruence factor results in terms of uncertainties and sensitivities towards the electrical conductivities of brain tissues, fractional anisotropy, and measurement inaccuracies for all subjects of Experiment II considering the 6-of-20 case described previously. The results from subject S1 are shown in Fig. 10. The results of subject S8 and S12 are shown in Fig. S5 and Fig. S6 in the *Supplemental Material*. The uncertainties of the model parameters are listed in Table 1, as well as in Table S1 and Table S2 in the *Supplemental Material.* The spatial distributions of the mean, the relative standard deviation (*RSD*), and the variance (*VAR*) of the congruence factor are shown in Fig. 10(a). The mean distribution shows a hotspot, which is extending from the gyral crown of M1 to upper parts of the anterior sulcal wall. The *RSD* and *VAR* indicate that on the gyral crown, the congruence factor can be determined with a greater certainty ($RSD \approx 12\%$) than the one on the anterior sulcal wall ($RSD \approx 40\%$).

In order to identify the most influential model parameters, we decomposed *VAR* into its origins by a Sobol decomposition. The spatial distributions of the absolute first order Sobol indices on the cortex are shown in Fig. 10(b). The Sobol coefficient maps of the MEP curve parameters are accumulated to one Sobol index termed Sobol (EXP). The average first and highest second order Sobol indices are depicted in Fig. 10(c) for all subjects of Experiment II. The average was computed over the elements in the ROI. For all subjects, it can be observed that the most protrude parameters that contribute to the uncertainty of the congruence factor are the electrical conductivities of GM (σ_{GM}), WM (σ_{WM}) as well as the uncertainty of the measured MEP curves (exp). Their relative contribution to the total variance, shown in Fig. 10(d) (and in the *Supplemental Material* Fig. S5(d) and Fig. S6(d)), is subject specific and depends on the accuracy of the measured MEP curves as well as on the brain anatomy, influencing the electric field distribution. It can be observed that the uncertainty of the congruence factor hotspot in the anterior sulcal wall predominantly originates from the uncertainty of σ_{GM} and the measurement uncertainties.

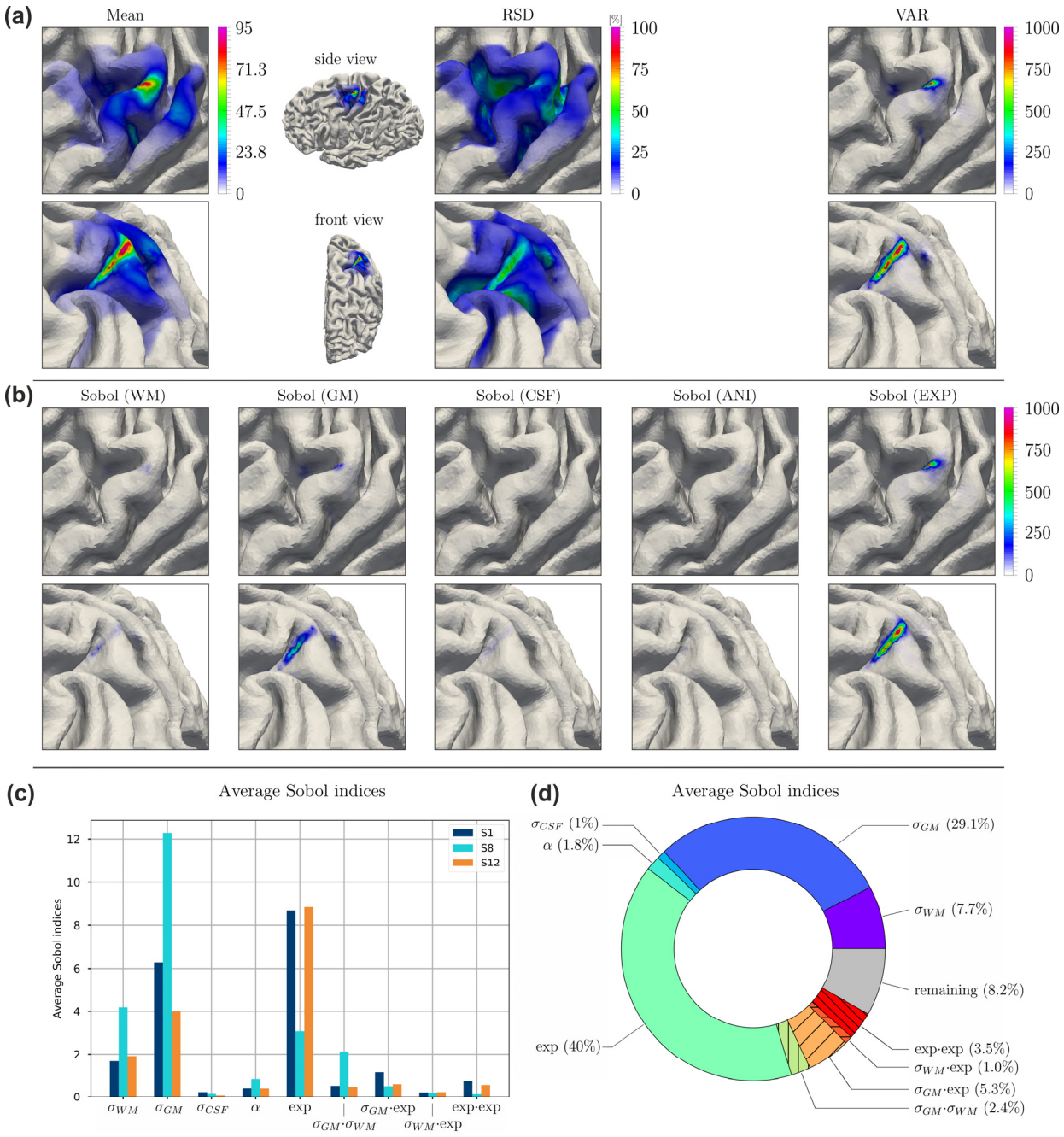

Figure 10: Uncertainty and sensitivity analysis of the congruence factor determined for subject S1 in the 6-of-20 analysis of Experiment II. (a) Expected value (Mean), relative standard deviation (RSD), and variance (VAR) of the congruence factor. (b) Spatial distributions of the absolute first order Sobol indices. The normalization with respect to the total variance was avoided to strengthen the focus on regions of high variance (see eq. (12) in the *Supplementary Material* on how the Sobol indices are computed). The Sobol index maps of the individual MEP parameters resulting from uncertainties in the experimental data are summarized into one Sobol index map "Sobol (EXP)". (c) Average first order Sobol indices for subjects S1 (shown here), S8, and S12. The average was computed over the elements in the ROI (d) Relative first order Sobol indices averaged over the ROI. For (a) and (b) two different perspectives are shown (top and bottoms rows), in order to improve visibility of the effects.

527 **4 DISCUSSION**

528 In the present study, we introduce a novel approach that links numerical modeling of the
529 induced electric field with measurements of peripheral physiological responses to considerably
530 improve the localization of effectively stimulated areas during TMS. With this approach, we
531 were able to accurately localize the cortical area that is responsible for the observed motor
532 output when single TMS pulses were applied over the motor cortex. Our main finding was that
533 sharply bounded neural structures located in the gyral crowns extending to the upper parts of
534 the sulcal wall of the motor hand area represent the most likely origin of the motor evoked
535 potentials. We identified the magnitude and the tangential component of the electric field as
536 the relevant quantities for modulating the observed effect. Our results implicate that unique
537 results can be obtained with relatively few measurements. Based on our findings, we derive
538 principles for the selection of the respective coil positions that may help to improve localization
539 of TMS effects in future applications, both at the single subject and group level. Our first
540 experiment combined two different stimulation sites with three coil rotations each, yielding 6
541 conditions. The induced electric fields were computed with FEM, allowing for the assessment of
542 element-wise E-MEP relations. We identified three groups with a hotspot at either M1, the
543 somatosensory cortex, or both. One subject from each group was included in the extended
544 second experiment. Here, the number of experimental conditions was increased from 6 to 20,
545 considering 4 coil positions with 5 orientations. For the subject from the M1-group, the hotspot
546 was replicated at the same spot. For the subjects from the other two groups, the results could
547 be significantly improved and single hotspots at the gyral crowns and the upper parts of the
548 sulcal walls of the motor hand area could be observed in all cases. This result is well supported
549 by, and extends, previous modeling studies on the application of TMS to M1 (Bungert et al.,
550 2017; Laakso et al., 2018). In the present study, the employed congruence factor quantifies
551 the correlation between the measured physiological variable (here, the MEP) and the induced
552 electric field profiles. Note that the proposed approach does not depend on the involved
553 function types to describe the I/O behavior. This provides a high level of flexibility and makes
554 the method easily adaptable to other applications.

555 Based on the results of two experiments, we argue that areas with maximum congruence
556 factors are good candidates for effective stimulation. Importantly, we observed in all subjects

that higher variability between electric fields sharpened the localization results. Sets of experimental conditions that selectively varied coil position or coil orientation did not contain sufficient information to uniquely determine the effective cortical site of stimulation. Moreover, stimulation directly over M1 with 45° orientation, though yielding the strongest effect, was by far not the most informative condition in our method, which can be explained by the relative wide spread of the electric field in the motor area, and hence, with low discriminative power, produced by standard figure-of-eight coils. These observations might provide a potential explanation for the spurious second hotspot in the somatosensory cortex observed by Bungert et al. (2017) when stimulating selectively over M1 and Laakso et al. (2018), stimulating with a 45° coil orientation towards the fissure longitudinalis (Brasil-Neto et al., 1992). Interestingly, studies incorporating selectively this coil orientation (Laakso et al., 2018; Krieg et al., 2013; Salinas et al., 2011) appear to support sulcal wall activation by $|\mathbf{E}_{\perp}|$. In contrast, studies which involve different coil orientations (Bungert et al., 2017) highlight $|\mathbf{E}|$ and gyral crowns. Recent results from direct electric stimulation (Aonuma et al., 2018) support the hypothesis for gyral crown activation, which is in contrast to the conclusions drawn from applying imaging techniques (Fox et al., 2004; Krieg et al., 2013). However, both methods have the major disadvantage that their resolution in the current state of research is not sufficient to answer this question. By changing both, i.e. coil orientation and coil location, we observed low congruence factors for $|\mathbf{E}_{\perp}|$ at the anterior wall of the central sulcus. Since low congruence factors highlight areas where the behavioral effect does not correlate with changes in the local electric field, our results indicate that the previously proposed stimulation mechanism by $|\mathbf{E}_{\perp}|$ (Laakso et al., 2018; Fox et al., 2004; Krieg et al., 2013) cannot explain the observed effect for all experimental conditions. The hypothesis of the existence of multiple stimulation mechanisms is supported by the relatively high rate of non-responders (36.4%) observed by Fox et al. (2004) considering cerebral blood flow in positron emission tomography after successful TMS. We observed that the tangential component (and therefore also the magnitude) of the field showed reasonable congruence factor maps. Our finding suggests that the gyral crowns and upper parts of the sulcal wall are the most likely origin of the motor evoked potentials.

With respect to potential differences between our approach and previous studies, it should be noticed that Opitz et al. (2013) weighted the computed electric fields with the strengths of the observed effects and overlaid the fields in an additive fashion. In contrast, Aonuma et al. (2018) superimposed the fields multiplicatively after selecting the experimental conditions for which the observable effect exceeded a particular threshold. The latter may be disadvantageous since it uses only a small portion of the information contained in the measurement. Both methods approximate a covariance between the field strength and the MEP amplitude. However, this covariance does not only depend on the correlative relationship between the two, but also on the general magnitude of the field across conditions. This means there is a strong bias towards voxels which generally receive higher field strengths (i.e., on gyral crowns).

In accordance with our findings regarding the need of electric field variability, it was argued before that an exact localization of the cortical activation site was not possible due to spatial correlations of the induced electric fields (Laakso et al., 2018). This can be observed in Bungert et al. (2017, Fig. 4a) as well as in Laakso et al. (2018, Fig. 5). We also observed similar effects in Experiment I, where only 5 or 6 non-optimal experimental conditions were considered (subject group II and III, Fig. 7). Reducing the correlation of the electric fields (Experiment II), we were able to considerably enhance the localization capabilities of our method in all subjects. This observation was further supported by a permutation analysis showing that higher variability between the spatial patterns of the electric fields, by means of using particular combinations of coil positions and orientations, considerably increases the accuracy of the localization results.

The uncertainty and sensitivity analyses confirmed robust hotspots on the gyral crowns extending to upper parts of the sulcal wall of M1 (cf. Fig. 10, Fig. S5, and Fig. S6). The maxima of the mean coincides well with the results of the deterministic case omitting any randomness (cf. Fig. 9). The relative standard deviation (RSD) in the hotspots on the gyral crown varies between 10-25%, depending on the subject. The spatial profile of the variance is similar to the mean, which indicates that the general profile of the congruence factor and thus, the location of the hotspot is stable. Decomposing the variance into their origins revealed a

strong contribution from GM and WM conductivity as well as from the measured I/O curves. However, the uncertainties mainly translate into uncertainties of the congruence factor on the anterior sulcal wall of the precentral gyrus and not on the gyral crown, where the primary hotspot was detected.

This is in line with previous studies, which showed that the electrical conductivities of GM and WM are the most influencing parameter considering the induced electric field in grey matter (Weise et al., 2015; Codecasa et al., 2016; Saturnino et al., 2018). The impact of the measurement uncertainty was lower for subject S8 compared to the other subjects, which can be explained by the fact that the MEP curves could be determined with a higher certainty (cf. Table 1, S1, and S2). Nevertheless, its contribution is still high and special care should be taken when recording characteristic regions of the I/O curve, like the turning points of the sigmoids, to reduce its influence on the congruence factor. In contrast, the conductivity of CSF and the level of anisotropy have a small impact on the congruence factor and could be treated as deterministic in future analyses.

Combining electric field computations and compartment models of neurons, Seo et al. (2017) propose the initial segments of pyramidal cells in layer 3 and 5 to be the sites of effective stimulation, possibly due to the omnidirectional orientation of the basal dendritic trees. Alternatively, also the terminals of axon collaterals might be stimulated (Aberra et al., 2018), which again are equally distributed in all directions around the main axon and have low thresholds. Our results, namely high congruence factors of the magnitude and the tangential component of the electric field in the gyral crown and rim indicate that the stimulation mechanism of TMS may indeed occur due to synaptic or dendritic activation of neurons. This is in line with predictions from previous modeling studies (Silva et al., 2008; Salvador et al., 2011). Future studies may extend the congruence factor approach to more detailed neuron models (Moezzi et al., 2018) and tractography-based fiber tracts (De Geeter et al., 2015; De Geeter et al., 2016).

In order to enable clinical applicability of the proposed method, for instance in presurgical mapping, the experimental effort has to be reduced to a minimum while ensuring reliability. Regarding our second research question, the permutation analysis from Experiment II (Fig. 8, Fig. S3, and Fig. S4) revealed that six stimulation conditions at three different locations around

M1 with different orientations are sufficient to address the localization problem at hand. Notably, the actual condition combinations that result in a minimum hotspot area differ strongly between subjects. This is due to inter-individual differences in anatomy and functional brain organization. Using a high number of experiments increases the stability and reliability of the solution. However, at the same time, it also reduces the resolution by introducing more measurement uncertainty. This became evident in the permutation study in Fig. 8(b), where the minimal hotspot area has a minimum for $k = 6$ conditions and slightly increases for higher values of k. Increasing the field variability is promising starting point for subject specific optimization to determine the optimal number and selection of coil positions and orientations beforehand. An even more sophisticated scheme could involve maximizing the distinguishability between voxels based on their sensitivity profiles, that is, the vectors of E fields caused by the different coil positions and orientations with identical activation strength. In order to distinguish two voxels with respect to their congruence factor, their sensitivity profiles should be as different as possible. The formulation of an optimization procedure that identifies the best combination of coil positions and orientations to maximize the differences of the sensitivity profiles between any two voxels in the region of interest will be investigated in detail in future research.

Beyond the localization of the origin of MEPs, our approach allows to localize functionally involved cortical areas for other processes, provided that it is possible to observe a quantitative response variable that depends on the stimulation intensity. Considering adapted experimental paradigms, which are able to capture this, future studies may use our approach for presurgical language mapping purposes. Alternatively, paired pulse TMS experiments of the somatosensory cortex may be used to investigate intracortical inhibition and facilitation of the motor cortex (Oliveri et al., 2000; Koch et al., 2006).

So far, our method relies on the assumption that the experimental effects can be explained by activity in a single cortical patch. This holds in the current motor experiment identifying the cortical origin of FDI activation. In other experimental paradigms however, there may exist several network nodes that, if stimulated, influence the effect. These nodes may also influence each other in different ways. This would lead to partial correlations. Incorporating connections will tremendously increase the computational cost and efficient algorithms have to be used to

combine the electric field profiles and the physiological response data. Since numerous connections can be analyzed independently from each other, the problem is highly parallelizable and well suited for GPU or HPC implementations. The extension of our technique to identify multivariate relationships between externally observable effects and stimulation of neural populations is subject of ongoing work.

We conclude that our approach improves the localization of effectively stimulated areas during TMS and may increase the power and reliability of the resulting effects in future TMS studies at the individual level.

Acknowledgments

Konstantin Weise; Max Planck Institute for Human Cognitive and Brain Sciences, Stephanstr. 1a, 04103 Leipzig, Germany; Technische Universität Ilmenau, Advanced Electromagnetics Group, Helmholtzplatz 2, 98693 Ilmenau, Germany; e-mail: kweise@cbs.mpg.de, phone: +49 341 9940-2580. This work was partially supported by the German Science Foundation (DFG) (grant number WE 59851/1); Lundbeckfonden (grant no. R118-A11308), the NVIDIA Corporation and NovoNordisk fonden (grant no. NNF14OC0011413).

References

Aberra, AS, Peterchev AV, Grill WM. Biophysically realistic neuron models for simulation of cortical stimulation. J. Neural Eng. 2018; 15(6):66023. (doi: 10.1088/1741-2552/aadbb1)

Akaike, H. A new look at the statistical model identification. IEEE Trans. Automat. Contr. 1974; 19(6):716-723. (doi: 10.1109/TAC.1974.1100705)

Akhtari M, Mandelkern M, Bui D, Salamon N, Vinters HV, Mathern GW. Variable anisotropic brain electrical conductivities in epileptogenic foci. Brain Topogr 2010; 23(3):292-300. (doi: 10.1007/s10548-010-0144-z)

Aonuma S, Gomez-Tames J, Laakso I, Hirata A, Takakura T, Tamura M, Muragaki Y. A high-resolution computational localization method for transcranial magnetic stimulation mapping. NeuroImage 2018; 172(1):85–93. (doi: 10.1016/j.neuroimage.2018.01.039)

Askey R, Wilson JW. Some Basic Hypergeometric Orthogonal Polynomials that Generalize Jacobi-Polynomials. Mem Amer Math Soc 1985; 54(319):1–55. (ISBN: 9780821860557)

Baumann SB, Wozny DR, Kelly SK, Meno FM. The Electrical Conductivity of Human Cerebrospinal Fluid at Body Temperature. IEEE Trans Biomed Eng 1997; 44(3):220-223. (doi: 10.1109/10.554770)

Bestmann S. The physiological basis of transcranial magnetic stimulation. Trends Cogn Sci 2008; 12: 81-83. (doi: 10.1016/j.tics.2007.12.002)

Bestmann S. Computational neurostimulation in basic and translational research. Prog Brain Res 2015; 222: xv-xx. (doi: 10.1016/S0079-6123(15)00159-4)

Bestmann S, Feredoes E. Combined neurostimulation and neuroimaging in cognitive neuroscience: past, present, and future. Ann N Y Acad Sci 2013; 1296: 11-30. (doi: 10.1111/nyas.12110)

Bikson M, Truong DQ, Mourdoukoutas AP, Aboseria M, Khadka N, Adair D, Rahman A. Modeling sequence and quasi-uniform assumption in computational neurostimulation. Prog Brain Res 2015; 222: 1-23. (doi: 10.1016/bs.pbr.2015.08.005)

Brasil-Neto JP, Cohen LG, Panizza M, Nilsson J, Roth BJ, Hallett, M (1992). Optimal focal transcranial magnetic activation of the human motor cortex: effects of coil orientation, shape of the induced current pulse, and stimulus intensity. Journal of clinical neurophysiology 9(1), 132-136. (PMID: 1552001)

Bungert A, Antunes A, Espenhahn S, Thielscher A. Where does TMS Stimulate the Motor Cortex? Combining Electrophysiological Measurements and Realistic Field Estimates to Reveal the Affected Cortex Position. Cereb Cortex 2017; 27: 5083-5094. (doi: 10.1093/cercor/bhw292)

Codecasa L, Di Rienzo L, Weise K, Gross S, Haueisen J. Fast MOR-based Approach to Uncertainty Quantification in Transcranial Magnetic Stimulation. IEEE Trans Magn 2016; 52(3):7200904. (doi: 10.1109/TMAG.2015.2475120)

Conforto AB, Z'Graggen WJ, Kohl AS, Rösler KM, Kaelin-Lang A. Impact of coil position and electrophysiological monitoring on determination of motor thresholds to transcranial magnetic stimulation. Clin Neurophysiol 2004; 115(4): 812-819. (doi: 10.1016/j.clinph.2003.11.010)

Datta A, Bikson M, Fregni F. Transcranial direct current stimulation in patients with skull defects and skull plates: high-resolution computational FEM study of factors altering cortical current flow. Neuroimage 2010; 52: 1268-1278. (doi: 10.1016/j.neuroimage.2010.04.252)

Dale AM, Fischl B, Sereno MI. Cortical surface-based analysis. I. Segmentation and surface reconstruction. NeuroImage 1999; 9(2): 179-194. (doi: 10.1006/nimg.1998.0395)

De Geeter N, Crevecoeur G, Leemans A, Dupré L. Effective electric fields along realistic DTI-based neural trajectories for modelling the stimulation mechanisms of TMS. Physics in medicine and biology 2015; 60(2): 453-471. (doi: 10.1088/0031-9155/60/2/453)

De Geeter N, Dupré L, Crevecoeur G. Modeling transcranial magnetic stimulation from the induced electric fields to the membrane potentials along tractography-based white matter fiber tracts. J. Neural Eng. 2016a; 13(2):26028. (doi: 10.1088/1741-2560/13/2/026028)

De Geeter, N, Lioumis, P, Laakso A, Crevecoeur G, Dupre L. How to include the variability of TMS responses in simulations: a speech mapping case study. Physics in medicine and biology 2016b; 61(21): 7571-7585. (doi: 10.1088/0031-9155/61/21/7571)

De Lucia M, Parker GJ, Embleton K, Newton JM, Walsh V. Diffusion tensor MRI-based estimation of the influence of brain tissue anisotropy on the effects of transcranial magnetic stimulation. Neuroimage 2007; 36: 1159-1170. (doi: 10.1016/j.neuroimage.2007.03.062)

Di Lazzaro V, Profice P, Ranieri F, Capone F, Dileone M, Oliviero A, Pilato F (2012). I-wave origin and modulation. Brain Stimulation 5(4). (doi: 10.1016/j.brs.2011.07.008)

Di Lazzaro V, Rothwell JC (2014). Corticospinal activity evoked and modulated by non-invasive stimulation of the intact human motor cortex. J Physiol 592(19). (doi: 10.1113/jphysiol.2014.274316)

Fischl B, Sereno MI, Dale AM. Cortical surface-based analysis. II: Inflation, flattening, and a surface-based coordinate system. NeuroImage 1999; 9(2): 195-207. (doi: 10.1006/nimg.1998.0396)

Fox PT, Narayana S, Tandon N, Sandoval H, Fox SP, Kochunov P, Lancaster JL. Column-based model of electric field excitation of cerebral cortex. Hum Brain Mapp 2004; 22: 1-14. (doi: 10.1002/hbm.20006)

Gabriel C, Peyman A, Grant EH. Electrical conductivity of tissue at frequencies below 1 MHz. Phys Med Biol 2009; 54(16):4863-4878. (doi: 10.1088/0031-9155/54/16/002)

Ghanem R, Higdon D, Owhadi H. Handbook of Uncertainty Quantification. Cham: Springer; 2016. (doi: 10.1007/978-3-319-12385-1)

Güllmar D, Haueisen, J, Reichenbach, JR. Influence of anisotropic electrical conductivity in white matter tissue on the EEG/MEG forward and inverse solution. A high-resolution whole head simulation study. NeuroImage 2010; 51(1): 145-163. (doi: 10.1016/j.neuroimage.2010.02.014)

Hallett M. Transcranial magnetic stimulation and the human brain. Nature 2000; 406: 147-150. (doi: 10.1038/35018000)

Hamada M, Murase N, Hasan A, Balaratnam M, Rothwell JC. The role of interneuron networks in driving human motor cortical plasticity. Cereb Cortex 2013; 23: 1593-1605. (doi: 10.1093/cercor/bhs147)

Hartwigsen G, Bergmann TO, Herz DM, Angstmann S, Karabanov A, Raffin E, Thielscher A, Siebner HR (2015). Modeling the effects of noninvasive transcranial brain stimulation at the biophysical, network, and cognitive Level. Prog Brain Res; 222: 261-287. (doi: 10.1016/bs.pbr.2015.06.014)

Jenkinson M, Beckmann CF, Behrens TE, Woolrich MW, Smith SM. FSL. NeuroImage 2012; 62(2): 782-790. (doi: 10.1016/j.neuroimage.2011.09.015)

Koch G, Franca M, Albrecht UV, Caltagirone C, Rothwell JC. Effects of paired pulse TMS of primary somatosensory cortex on perception of a peripheral electrical stimulus. Experimental brain research 2006; 172(3):416-424. (doi: 10.1007/s00221-006-0359-0)

Krieg TD, Salinas FS, Narayana S, Fox PT, Mogul DJ. PET-based confirmation of orientation sensitivity of TMS-induced cortical activation in humans. Brain Stimulation 2013; 6(6):898-904. (doi: 10.1016/j.brs.2013.05.007)

Krieg, S, Tarapore PE, Picht T, Tanigawa N, Houde J, Sollmann N, Meyer B, Vajkoczy P, Berger SB, Ringel F, Nagarajan S. Optimal timing of pulse onset for language mapping with navigated repetitive transcranial magnetic stimulation. NeuroImage 2014; 100, 219–236. (doi: 10.1016/j.neuroimage.2014.06.016)

Laakso I, Murakami T, Hirata A, Ugawa Y. Where and what TMS activates: Experiments and modeling. Brain Stimul 2018; 11: 166-174. (doi: 10.1016/j.brs.2017.09.011)

Le Maitre OP, Knio OM. Spectral Methods for Uncertainty Quantification. Dordrecht: Springer, 2010. (doi: 10.1007/978-90-481-3520-2)

Li C, Bak AF, Parker LO. Specific resistivity of the cerebral cortex and white matter. Exp Neurol 1968; 20(4):544-557. (doi: 10.1016/0014-4886(68)90108-8)

Logothetis NK, Kayser C, Oeltermann A. In vivo measurement of cortical impedance spectrum in monkeys: implications for signal propagation. Neuron 2007; 55(5):809-823. (doi: 10.1016/j.neuron.2007.07.027)

Mayka MA, Corcos DM, Leurgans SE, Vaillancourta DE. Three-dimensional locations and boundaries of motor and premotor cortices as defined by functional brain imaging. A meta-analysis. Neuroimage 2006; 31(4): 1453–1474. (doi: 10.1016/j.neuroimage.2006.02.004)

Miniussi C, Harris JA, Ruzzoli M. Modelling non-invasive brain stimulation in cognitive neuroscience. Neurosci Biobehav Rev 2013; 37: 1702-1712. (doi: 10.1016/j.neubiorev.2013.06.014)

Moezzi, B Schaworonkow N, Plogmacher L, Goldsworthy MR, Hordacre B, Mcdonnell M, Iannella N, Ridding MC, Triesch, J (2018). Simulation of electromyographic recordings following transcranial magnetic stimulation. Journal of neurophysiology. (doi: 10.1152/jn.00626.2017)

Neggers SF, Petrov PI, Mandija S, Sommer IE, van den Berg NA. Understanding the biophysical effects of transcranial magnetic stimulation on brain tissue: the bridge between brain stimulation and cognition. Prog Brain Res 2015; 222: 229-259. (doi: 10.1016/bs.pbr.2015.06.015)

Nicholson PW. Specific impedance of cerebral white matter. Exp Neurol 1965; 13(4):386-401. (doi: 10.1016/0014-4886(65)90126-3)

Oliveri M, Caltagirone C, Filippi MM, Traversa R, Cicinelli P, Pasqualetti P, Rossini PM. Paired transcranial magnetic stimulation protocols reveal a pattern of inhibition and facilitation in the human parietal cortex. The Journal of physiology 2000; 529(2): 461-468. (doi: 10.1111/j.1469-7793.2000.00461.x)

Oldfield, R.C., 1971. The assessment and analysis of handedness: The Edinburgh inventory. Neuropsychologia 9, 97–113. (doi:10.1016/0028-3932(71)90067-4)

Opitz A, Legon W, Rowlands A, Bickel WK, Paulus W, Tyler WJ. Physiological observations validate finite element models for estimating subject-specific electric field distributions induced by transcranial magnetic stimulation of the human motor cortex. Neuroimage 2013; 81: 253-264. (doi: 10.1016/j.neuroimage.2013.04.067)

Opitz A, Windhoff M, Heidemann RM, Turner R, Thielscher A. How the brain tissue shapes the electric field induced by transcranial magnetic stimulation. Neuroimage 2011; 58: 849-859. (doi: 10.1016/j.neuroimage.2011.06.069)

Opitz, A., Legon, W., Rowlands, A., Bickel, W. K., Paulus, W., & Tyler, W. J. (2013). Physiological observations validate finite element models for estimating subject-specific electric field distributions induced by transcranial magnetic stimulation of the human motor cortex. NeuroImage, 81, 253-264. (doi: 10.1016/j.neuroimage.2013.04.067)

Opitz A, Zafar N, Bockermann V, Rohde V, Paulus W. Validating computationally predicted TMS stimulation areas using direct electrical stimulation in patients with brain tumors near precentral regions. NeuroImage. Clinical 2014; 4: 500-507. (doi: 10.1016/j.nicl.2014.03.004)

Pascual-Leone A, Torres F. Plasticity of the sensorimotor cortex representation of the reading finger in Braille readers. Brain 1993; 116(1): 39-52. (PMID: 8453464)

Penny W, Friston K, Ashburner J, Kiebel S, Nichols T. Statistical Parametric Mapping: The Analysis of Functional Brain Images, Academic Press, 2007, 1st Edition (ISBN 9780123725608)

Picht, T. (2014). Current and potential utility of transcranial magnetic stimulation in the diagnostics before brain tumor surgery. CNS oncology, 3(4), 299-310. (doi: 10.2217/cns.14.25)

Ranck JB. Specific impedance of rabbit cerebral cortex. Exp Neurol 1963; 7:144-152. (doi: 10.1016/S0014-4886(63)80005-9)

Rossi, S., Hallett, M., Rossini, P.M., Pascual-Leone, A., 2009. Safety, ethical considerations, and application guidelines for the use of transcranial magnetic stimulation in clinical practice and research. Clin. Neurophysiol. 120, 2008–39. (doi:10.1016/j.clinph.2009.08.016)

Rothwell JC, Hallett M, Berardelli A, Eisen A, Rossini P, Paulus W (1999). Magnetic stimulation: motor evoked potentials. Electroencephalogr Clin Neurophysiol Suppl, 52, 97-103. (PMID: 10590980)

Salinas FS, Szabó CÁ, Z W, Jones L, Leland MM, Wey HY, Duong TQ, Fox PT, Narayana S. Functional neuroimaging of the baboon during concurrent image-guided transcranial magnetic stimulation. NeuroImage 2011; 57(4):1393-1401. (doi: 10.1016/j.neuroimage.2011.05.065)

Salvador, R., Silva, S., Basser, P. J., & Miranda, P. C. (2011). Determining which mechanisms lead to activation in the motor cortex: a modeling study of transcranial magnetic stimulation using realistic stimulus waveforms and sulcal geometry. Clinical neurophysiology, 122(4), 748-758. (doi 10.1016/j.clinph.2010.09.022)

Sandrini M, Umilta C, Rusconi E. The use of transcranial magnetic stimulation in cognitive neuroscience: a new synthesis of methodological issues. Neurosci Biobehav Rev 2011; 35: 516-536. (doi: 10.1016/j.neubiorev.2010.06.005)

Saturnino, G., Thielscher, A., Madsen, K. H., Knösche, T. R., Weise, K. (2018). A principled approach to conductivity uncertainty analysis in electric field calculations. NeuroImage. in press. (doi: 10.1016/j.neuroimage.2018.12.053)

Seo H., Schaworonkow N., Jun S. C., Triesch J. (2017). A multi-scale computational model of the effects of TMS on motor cortex. *F1000Research* 2017, **5**:1945 (doi: 10.12688/f1000research.9277.3)

Siebner HR, Hartwigsen G, Kassuba T, Rothwell JC. How does transcranial magnetic stimulation modify neuronal activity in the brain? Implications for studies of cognition. Cortex 2009; 45: 1035-1042. (doi: 10.1016/j.cortex.2009.02.007)

Silva, S., Basser, P. J., & Miranda, P. C. (2008). Elucidating the mechanisms and loci of neuronal excitation by transcranial magnetic stimulation using a finite element model of a cortical sulcus. Clinical neurophysiology, 119(10), 2405-2413. (doi: 10.1016/j.clinph.2008.07.248)

Smith SM, Jenkinson M, Woolrich MW, Beckmann CF, Behrens TEJ, Johansen-Berg H, Bannister PR, De Luca M, Drobnjak I, Flitney DE, Niazy R, Saunders J, Vickers J, Zhang Y, De Stefano N, Brady JM, Matthews PM. Advances in functional and structural MR image analysis and implementation as FSL. NeuroImage 2004; 23(S1): 208-219. (doi: 10.1016/j.neuroimage.2008.10.055)

Sobol IM. Global sensitivity indices for nonlinear mathematical models and their Monte Carlo estimates. Math Comput Simulat 2001; 55(1-3):271-280. (doi: 10.1016/S0378-4754(00)00270-6)

Sudret B. Global sensitivity analysis using polynomial chaos expansions. Reliab Eng Syst Safe 2008; 93(7):964–979. (doi: 10.1016/j.ress.2007.04.002)

Tarapore, PE, Findlay AM, Honma SM, Mizuiri, D, Houde JF, Berger MS, & Nagarajan, SS. Language mapping with navigated repetitive TMS: Proof of technique and validation. NeuroImage 2013; 82:260–272. (doi: 10.1016/j.neuroimage.2013.05.018)

Thielscher A, Antunes A, Saturnino GB. Field modeling for transcranial magnetic stimulation: A useful tool to understand the physiological effects of TMS? Conf Proc IEEE Eng Med Biol Soc 2015; 222-225. (doi: 10.1109/EMBC.2015.7318340)

Thielscher A, Opitz A, Windhoff M. Impact of the gyral geometry on the electric field induced by transcranial magnetic stimulation. Neuroimage 2011; 54: 234-243. (doi: 10.1016/j.neuroimage.2010.07.061)

Tuch DS, Wedeen VJ, Dale AM, George JS, Belliveau JW. Conductivity tensor mapping of the human brain using diffusion tensor MRI. Proceedings of the National Academy of Sciences of the United States of America 2001; 98(20): 11697-11701. (doi: 10.1073/pnas.171473898)

Wagner TA, Zahn M, Grodzinsky AJ, Pascual-Leone A. Three-dimensional head model simulation of transcranial magnetic stimulation. IEEE Trans Biomed Eng 2004; 51(9): 1586-1598. (doi: 10.1109/TBME.2004.827925)

Weise K, Di Rienzo L, Brauer H, Haueisen J, Toepfer H. Uncertainty Analysis in Transcranial Magnetic Stimulation Using Non-intrusive Polynomial Chaos Expansion. IEEE Trans Magn 2015; 51(7):5000408. (doi: 10.1109/TMAG.2015.2390593)

Windhoff M, Opitz A, Thielscher A. Electric field calculations in brain stimulation based on finite elements: an optimized processing pipeline for the generation and usage of accurate individual head models. Hum Brain Mapp 2013; 34: 923-935. (doi: 10.1002/hbm.21479)

Woolrich MW, Jbabdi S, Patenaude B, Chappell M, Makni S, Behrens T, Beckmann C, Jenkinson M, Smith SM. Bayesian analysis of neuroimaging data in FSL. NeuroImage 2009; 45(S1): 173-86. (doi: 10.1016/j.neuroimage.2008.10.055)

Yedlin M, Kwan H, Murphy JT, Nguyen-Huu H, Wong YC. Electrical conductivity in cat cerebellar cortex. Exp Neurol 1974; 43(3):555-569. (doi: 10.1016/0014-4886(74)90195-2)